



Self-consistent surface-temperature boundary condition for liquefying-fuel-based hybrid rockets internal-ballistics simulation



Carmine Carmicino^{a,b,*}, Giuseppe Gallo^a, Raffaele Savino^a

^a Dipartimento di Ingegneria Industriale, Aerospace Division, Universitàdi Napoli "Federico II", P.le Tecchio 80, 80125 Napoli, Italy
^b Currently Baker Hughes, Via F. Matteucci 2, 50127, Firenze, Italy

ARTICLE INFO

Article history:

Received 8 September 2020

Revised 4 November 2020

Accepted 6 December 2020

Available online 23 January 2021

Keywords:

Hybrid rocket

Liquefying fuel

Pyrolysis model

Internal ballistics

Computational fluid dynamics

Fuel regression rate

ABSTRACT

A novel methodology for the calculation of the surface temperature of liquefying fuels typically burned in hybrid rockets is proposed. This procedure stems from the formulation of a fuel in-depth pyrolysis model coupled with the resolution of the thermo-fluid-dynamic field in the rocket combustion chamber, which allows for the characterization of the unstable liquid layer formed on top of the fuel surface. The aim is the simulation of the internal ballistics of hybrid rocket engines fed by paraffin-based fuels without the need for parametrically assigning the surface temperature to match the experimental data as, indeed, required in the authors' previous work. With the presented technique, surface temperature and fuel vaporization rate are calculated locally along the wall, and, with the integration of a liquid fuel entrainment model, which requires the tuning of just one parameter (i.e. the so-called entrainment factor), the fuel regression rate is determined. The overall numerical approach, upon the assumption that the liquid fuel is in the supercritical pressure regime, is based on the solution of the Reynolds-averaged Navier-Stokes equations for single-phase multicomponent turbulent reacting flow. A series of numerical simulations are carried out to unveil the effect of the oxygen mass flux, which allowed deriving an approximate analytical equation for the regression rate prediction. A set of hot fires of a laboratory-scale hybrid rocket are reproduced through single numerical simulations carried out on the fuel port average geometry in the burn to validate the computational model, showing deviations between the measured and predicted average regression rate less than 4.5%. In order to fairly match also the fuel consumption axial profile, transient numerical simulations over the entire engine firing are conducted with which the post-burn port shape is captured with maximum error of 8%.

© 2021 Elsevier Ltd. All rights reserved.

1. Introduction

In hybrid rocket engines propellants are stored in separate physical states and burn in the thrust chamber, where usually a hollow solid fuel grain is bonded, through a diffusive flame fed by the liquid oxidizer injected into the grain port and the fuel gasified for the heat developed by combustion [1]. This unique configuration, on the one hand, gives rise to improved system safety and significantly lower development costs but, on the other, poses several design challenges in that the engine performance prediction depends on the ability of mastering the fuel regression rate along with the propellant mixing and reaction processes.

A significant portion of the research carried out on hybrid rockets from about a decade involves the employment of liquefying

fuels [2] for their key property of regressing around three times faster than traditional polymeric fuels [3]. Such a class of fuels, by avoiding the low volumetric loading of tricky multi-port fuel grains, has been, thus, identified as a possible candidate for the solution to the notoriously low regression rate of conventional hybrid rockets for high-thrust missions [4], which might allow for extensive employment of this safer and cheaper chemical propulsion technology with competitive performance [5,6].

Paraffin wax has been considered primarily as a liquefying, high regression-rate fuel in the pioneering work in Ref. [7,8]. The fuel consumption mechanism of this material is, in fact, different from the pure gasification occurring in a standard polymer such as, among the most commonly used, high-density polyethylene (HDPE), hydroxyl-terminated polybutadiene (HTPB), and polymethylmethacrylate (PMMA), because it principally implicates the formation of a low-viscosity unstable melt layer on the burning surface, thereby fuel liquid droplets and/or filament-like structures are released and entrained into the main gas stream

* Corresponding author.

E-mail address: carmicin@unina.it (C. Carmicino).

Nomenclature

a	regression rate coefficient
a_{ent}	entrainment parameter
Br	Brinkman number
c	specific heat
D	fuel grain port diameter
E_a	activation energy
f	fuel mixture fraction
f^2	mixture fraction variance
G	mass flux per unit port cross-section area
H	specific enthalpy
h	liquid layer thickness
k	turbulent kinetic energy
L	fuel grain length
L_m	heat of fusion
\dot{m}	fuel mass flux
O/F	average overall mixture ratio
p	pressure
Pr_t	turbulent Prandtl number
\dot{q}	heat flux
\dot{Q}_p	volumetric pyrolysis heat source
\dot{r}	regression rate
R	universal gas constant
\mathcal{R}	Reynolds stress tensor
Re_t	turbulent Reynolds number
Sc_t	turbulent Schmidt number
S_m	mass source term
S_h	energy source term
t	time
t_b	burning duration
T	temperature
u	gas velocity
U	gas mean velocity in the port
v	gas velocity component normal to surface
x	generic coordinate, axial coordinate
y^+	dimensionless wall distance
Y	liquid fuel mass fraction
Y_j	mass fraction of the j -th species

Greek Symbols

α	thermal diffusivity
B	probability density function
B_p	pyrolysis frequency factor
δ	characteristic thermal layer thickness
Δ	grid node displacement
Δh_p	fuel heat of pyrolysis
ΔH_w	enthalpy difference between flame and wall
ΔM	fuel mass consumed
ε	turbulence dissipation rate
θ	fuel surface local inclination
λ	thermal conductivity
λ_g	gas thermal conductivity
μ	viscosity
μ_t	turbulent viscosity
ρ	density
ρ_g	average gas density in the grain port
σ	surface tension
τ	stress tensor
τ_g	mean shear stress at the wall
ω	turbulence specific dissipation rate
$\dot{\omega}_p$	fuel gas production rate
φ	generic function of enthalpy and mixture fraction
Ω	vorticity vector magnitude

ξ normal-to-surface coordinate

<i>Subscripts</i>	
c	critical
ent	entrainment component
f	fuel
l	liquid fuel
m	melting
ox	oxidizer
s	solid fuel
v	vaporization component
w	fuel surface
2	final
0	initial

Superscripts

$-$	time average
\sim	Favre average
$'$	fluctuation
\sim	local time average

[9,10,11]. The liquid entrainment is responsible for the observed fuel consumption-rate growth; as demonstrated with the aid of optical techniques by Petrarolo et al. [12], it is driven by the liquid layer hydrodynamic instability which originates from the shear flow in the combustion port, and, unlike the regression of the above-mentioned polymers, it is marginally affected by the heat transfer to the wall, so that it is not limited by the so-called blocking effect of the gas blowing from the surface [13]. The two main parameters affecting the instability, according to both experiments [12] and results of the linear stability theory [8], are the oxidizer mass flux in the port and the liquid fuel viscosity, i.e. the higher the mass flux and the lower the viscosity, the larger the entrainment is.

Usually, in order to improve the poor structural performance of paraffin-wax fuel grains, mechanical strengtheners are included into the fuel composition [14], which, however, alter the liquid fuel viscosity, and reduce the entrainment regression producing a major impact on motor performance. Overall, the entrainment process is influenced by the fuel composition and its thermo-mechanical properties [15,16] that can considerably change depending upon the specific fuel formulation, the manufacturing procedure and the motor operating conditions. As a consequence, the behaviour of paraffin-based fuels is hardly predictable [17] and requires, on the one hand, preliminary experimental campaigns on the material and, on the other, extended rocket static firings to measure the achievable engine performance. In this framework, the Computational Fluid Dynamics (CFD) applied to the prediction of the hybrid rocket internal ballistics is arousing an ever growing attention as a tool for containing the engine operation uncertainties as well as for easing the interpretation of experimental data, while the modelling capabilities are being further improved; a comprehensive review of the state of the art in this field is given in Ref. [18].

Regardless of the fuel type (standard polymers or liquefying materials) and oxidizer analysed, the vast majority of computational setups are based on the steady-state solution of the Reynolds Averaged Navier-Stokes (RANS) equations integrated with proper turbulence and combustion models [19]. Though, in principle, the fuel regression rate can be an input to the numerical simulation [20,21,22], for instance when one focuses on studying the propellant mixing and combustion processes in the motor [16], the case by far most interesting is the derivation of the fuel consumption from the resolution of the thermo-fluid-dynamic field. The latter task is tackled with the formulation of an ad-hoc solid fuel/gas

interface treatment relying on local mass, energy and species balances combined to either a pyrolysis-rate equation in the case of classical polymers [23,24], or to additional modelling for the evaluation of the entrained liquid fuel fraction contributing to the total fuel consumption rate. In fact, as mentioned above, the fuel entrained fraction is closely related to the structure of the unstable waves developing on the liquid fuel surface, as they play a central role in the mass and momentum transfer between the gas and liquid phases [25]. Thus, successful simulation in this area needs modelling the waves' characteristics. Of course, this latter target, coupled with the simulation of two-phase turbulent reacting flow in the combustion chamber, requires huge computational efforts, so that suitable simplifying strategies are employed to make the computations affordable.

Efforts devoted to gas/fuel surface modelling for paraffin-based hybrid rockets are, however, still rare. A couple of them, on the one hand, are aimed at the investigation of the liquid layer instability but ignore combustion. The work in Ref. [26] reports on the results of direct numerical simulations of a simple Couette flow to study the dynamics of a liquid film of methane in supercritical conditions attempted to resembling what actually occurs in the motor operation with paraffin-based fuel. In Ref. [27] a commercial package is used to simulate the laminar flow field ensuing from air flowing on a slab of liquid paraffin wax, to study the structure of the velocity field near the liquid layer with the formation and mass transfer rate of liquid droplets entrained in the main flow. In both cases, it was found that increasing velocity leads to increased entrainment. On the other hand, combustion is accounted for, but the details of the melted layer break up and subsequent liquid paraffin injection in the flow field are disregarded based on the consideration that, under the rocket chamber operating conditions, the melted paraffin wax is in the supercritical pressure regime, for which surface tension vanishes and the neat distinction between gas and liquid phases disappears; thus the entrainment is treated as part of the turbulent mixing process [28,29]. In the latter two references, finite-rate chemistry is employed with global reaction mechanisms including a thermal cracking reaction step for paraffin wax; the heat flux to the wall included the radiation contribution from the gas species (the effect of soot radiation was not taken into account), and the solid surface temperature was assumed equal to the paraffin wax melting temperature, regardless of the operating conditions. Predicted average regression rates on two laboratory-scale motors tested in different institutions (NASA Ames and University "Federico II") were in the range of $\pm 25\%$; however, it has to be remarked that all over the nine analysed test cases, the calculated radiation was a huge portion of the total heat flux reaching up to about 88% [29]. The same authors, in a later work [30], on the assumption that the fuel material is dominantly removed by the entrainment phenomena (i.e. the vaporization regression is negligible), calculated the entrainment fraction of regression rate by arbitrarily varying the wall temperature between the values of the paraffin wax melting and boiling points. The mentioned models still can display unacceptable deviations from experimental data, which, in some instances, are around 78% [31].

In a previous article of some of the present authors [32], they proposed a comprehensive model incorporating both a simplified description of gas/fuel surface interaction and combustion for the simulation of the internal ballistics of hybrid rockets fed with paraffin-based fuels; the main difference with respect to the above cited works is that the regression rate was assumed equal to the sum of the vaporization and entrainment fractions. A semi empirical correlation was utilized to calculate the regression rate component due to the liquid fuel entrainment. This latter, which will be detailed later, depends on the fuel properties through an entrainment parameter that was calculated parametrically together

with the fuel surface temperature (which was an arbitrary input to the problem) to match the regression rate experimentally measured. Despite the good agreement of the numerical results with the experimental data (less than 11% deviation on the time-space averaged regression rate), the model was dramatically sensitive to the choice of the surface temperature value, which was retained constant along the grain. The input of that temperature allowed neglecting the modelling of pyrolysis occurring in the melt layer, and the problem was reduced to the solution of the energy balance equation at the fuel wall for the calculation of the two distinct fractions of the total regression rate.

This paper addresses an improvement of the previous model thanks to which, by solving the heat conduction equation in both the liquid and solid fuel regions coupled to an in-depth pyrolysis reaction mechanism, allows calculating the surface temperature on a physical basis as part of the thermo-fluid-dynamic field resolution. The latter represents the second step along a logical path for an accurate description of the entrainment phenomenon: the first was employing a simplified entrainment correlation coupled with constant wall temperature; the current second step was the calculation of the surface temperature and the application of the same slightly improved entrainment correlation; the third future step is the modification of the entrainment model to overcome the limits described in what follows.

A set of experimental data, which were gathered from ground firings of a small-scale laboratory hybrid rocket carried out at the University of Naples "Federico II", is considered for the numerical model validation. The agreement between test data and computational results is excellent in terms of average fuel regression rate and can be even improved by a finer tuning of the model free parameter, whereas the measured fuel axial consumption profile deviates more significantly from the calculated one. The simplification introduced by carrying out just one CFD simulation on the time and space average port geometry is identified as the main reason behind the observed disagreement; a series of quasi-steady state numerical simulations are performed over the firing duration of a reference test to demonstrate that also the consumption profile can be captured with acceptable accuracy at the expense of the associated computational demand.

2. Numerical apparatus

In this section the full numerical approach is discussed with focus on modelling the phenomena occurring at the interface between the gas and liquid/solid fuel which is required for the fuel regression rate calculation. A summary of the numerical set up is given, without presenting the details of the equations solved that can yet be found in [Appendix A](#) for the sake of readers' convenience.

2.1. Thermo-fluid-dynamic model

Fuel grain material is here assumed to be composed by 100% paraffin wax with carbon number equal to 32 (i.e. with chemical formula: $C_{32}H_{66}$). The critical pressure of such a paraffin wax is 6.5 bar [33], thus, in the usual hybrid rocket chamber operating conditions the melted paraffin wax is in the supercritical pressure regime, for which surface tension disappears and the gas and liquid phases at the droplets surface tend to be undistinguishable; furthermore, viscosity and diffusivity are comparable to those typical of a gas, thereby the diffusion processes are significantly faster than in the liquid phase, which in a first approximation allows neglecting the two-phase flow effects. Accordingly, the RANS equations for a single-phase multicomponent turbulent reacting flow are solved in a two-dimensional axisymmetric domain

by means of a finite volume technique and a pressure-based algorithm [34]; as the chemical and fluid-dynamic characteristic times are much shorter than the fuel-regression time scale, steady-state solutions are sought [19]. Turbulence is described via the Shear Stress Transport (SST) model [35]. In the hybrid rocket combustion chamber, fuel and oxidizer burn in a diffusive flame, for which a non-premixed combustion model is employed. On the assumption that the chemical kinetics is fast compared to the diffusion processes occurring in the motor for the typical mass fluxes and chamber pressures considered here [36], the turbulence-chemistry interaction is modelled by means of the Probability Density Function (PDF) approach coupled to chemical equilibrium [37]. Under the hypothesis that all the chemical species considered have the same diffusivities, and assuming that the Lewis number is equal to 1, the species equations are reduced to just one equation for the transport of the mixture fraction.

The selected shape of the PDF is based on the beta distribution [38] and is function of the mean mixture fraction and its variance. For the model closure, an additional equation for the mixture-fraction variance is needed, which is formulated according to Ref. [39]. Finally, as the fluid system is non-adiabatic (heat is exchanged at the fuel surface), temperature and species of the reacting flow at the chemical equilibrium are affected by the heat loss, which requires solving the energy equation. Here, the enthalpy form of the energy equation is selected for the obvious benefit connected with the equilibrium calculations (which are carried out at constant enthalpy and pressure). Mean temperature and individual species mole fractions are then obtained by integration with the PDF, as functions of the mean mixture fraction, its variance and of the specific enthalpy. Chemical equilibrium conditions are calculated via the minimization of the Gibbs free energy algorithm [40] in a number of mixture fraction, mixture-fraction variance and enthalpy points at the chamber pressure value (which has been assumed equal to that measured in the firings), and a look up table is constructed. Thus, once the mean mixture fraction, its variance and mean enthalpy are calculated at each point in the flow field, the corresponding time-averaged species mole fractions, temperature and density are obtained interpolating the values in the lookup table. The density field is, then, scaled with the values of the actual pressure field in the system.

Heat capacities, molecular weights, and enthalpies of formation for each species considered are extracted from the chemical database in Ref. [40]; the mixture specific heat is determined via the mixing law. Molecular dynamic viscosities and thermal conductivities of the mixture are calculated as functions of local temperature according to Ref. [40].

2.2. Gas/liquefying fuel interface treatment

A scheme of the liquefying-fuels typical consumption mechanism is shown in Fig. 1. In the supercritical regime, part of the molten fuel on the solid surface is subjected to thermal decomposition and vaporization (i.e. pyrolysis), and part is lifted off from the surface in the form of a supercritical fluid (which, for the sake of simplicity, here is called "liquid") that is entrained in the gas stream and burns farer from the wall. In a certain sense, pyrolysis acts in the supercritical regime similarly to vaporization in the subcritical one, except for the surface temperature which is dictated by the pyrolysis process. Based on this observation, according to Ref. [7], the fuel regression rate, \dot{r} , is assumed equal to the sum of two terms, i.e. the vaporization fraction, \dot{r}_v , determined by pyrolysis, and the entrainment fraction, \dot{r}_{ent} , related to the mechanical transfer of the liquid from the surface:

$$\dot{r} = \dot{r}_v + \dot{r}_{ent} \quad (1)$$

Note that this simple superposition of the two separate effects of liquid entrainment and vaporization can be derived from simplifying the mass balance at the wall for which:

$$\rho_s \dot{r} = \dot{m}_v + \dot{m}_{ent} + \frac{d\dot{m}_l}{dx} \quad (2)$$

where $d\dot{m}_l/dx$ is the axial variation of the melted fuel mass flow rate per unit perimeter of the port in the direction parallel to the fuel grain surface (which is neglected), \dot{m}_v and \dot{m}_{ent} are the mass fluxes of the vaporized and entrained liquid, respectively. Eq. (1) can be, then, derived from Eq. (2) neglecting the change of fuel density with respect to the one in the solid state.

For the calculation of the regression rate and its two components, along with the resulting fuel mass fluxes, a set of equations needs to be formulated, whose solution is incorporated in the overall fluid dynamic computation. The required equations are derived essentially from stating the energy balance at the wall and a model for the liquid entrainment.

In the previous paper [32], assuming that the pyrolysis process was concentrated in a thin layer overlaying the liquid sheet and having thickness much smaller than the latter, the heat balance was formulated as follows:

$$\begin{aligned} \dot{q}_w &= - \left(\lambda_g \frac{\partial T}{\partial \xi} \right)_w \\ &= \rho_s \dot{r} [c_s(T_m - T_a) + L_m + c_l(T_w - T_m)] + \rho_s \dot{r}_v \Delta h_p \end{aligned} \quad (3)$$

where \dot{q}_w is the convective heat flux to the wall (here the radiation contribution to the heat exchanged at the wall is ignored), λ_g the gas thermal conductivity, ρ_s is the solid fuel density, c_s and c_l are the specific heats of the solid and liquid fuel, respectively, T_m is the fuel melting temperature, and L_m and Δh_p are the fuel heat of fusion and heat of pyrolysis, respectively; ξ is a coordinate normal to surface oriented from the gas to solid. Eq. (3) states that the heat transferred from the combusting gases to the fuel surface must be equal to the total of the heat conducted into the liquid layer (which is expressed by the sum of terms in the square brackets on the right-hand-side) plus the energy required by the fuel vaporized fraction for pyrolysis (last term on the right-hand-side). Wall temperature, T_w , has a significant influence on the fuel regression rate, as it affects both the heat flux to the surface and the term $c_l(T_w - T_m)$ appearing in the wall energy balance in Eq. (3); as mentioned above, in the subcritical regime it is determined by the evaporation phenomenon and is sensitive to the chamber pressure (note that, in the latter case, the heat of pyrolysis Δh_p is replaced by the heat of vaporization), whereas in the supercritical case it depends on the pyrolysis chemical reactions for which chamber pressure above the critical value does not play a role. It has to be remarked that, compared to purely pyrolyzing polymers, due to the effect of the liquid entrainment, which is the dominant fuel consumption mechanism, with hypothetically equal regression rate, the liquefying material shows lower surface temperature than a standard polymer, being vaporization only a fraction of the total regression rate. However, through Eq. (3) only, there is no means to determine the surface temperature, because of the lack of a relationship between pyrolysis data and fuel temperature. In fact, in Ref. [32], this parameter was calculated through a sensitivity analysis to match the experimental results, for which the value of 675 K was determined. By varying the surface temperature, it was observed that larger temperature yields both lower fuel vaporization and total regression rates, whereas the entrainment component is almost unchanged; this result was qualitatively confirmed later in Ref. [30]. In the following section, a model that correlates the surface temperature with the vaporization fraction of the regression rate, given a set of total regression rate and heat flux to the wall, is developed.

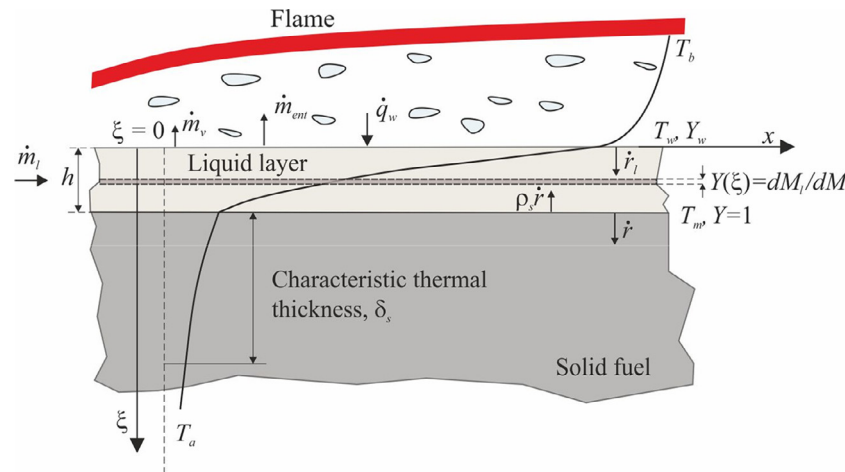


Fig. 1. Schematic of the typical fuel consumption mechanism and heat transfer across liquefying fuels.

2.2.1. Surface temperature calculation

A thermal analysis, which takes into account the chemical reactions occurring in the fuel bulk, is conducted to determine the surface temperature and the thickness of the melt layer. For the pyrolysis process, the mass fraction of the liquid fuel reduces from 1 to a lower value via thermal cracking of the original alkane molecules forming the fuel core. With the assumption that the fuel port radius is much larger than the overall thermal thickness across the fuel (their ratio is usually on the order of 10 or more), a semi-infinite slab of fuel is considered divided into the two zones shown in Fig. 1: the outer one is a thin layer of a supercritical fluid (supposed to have the same properties as paraffin in the liquid state) next to the solid surface, in which the pyrolysis reactions take place; in this zone the temperature varies from the wall temperature, T_w , to the melting temperature, T_m , and a fraction of the molten fuel undergoes pyrolysis while part is mechanically removed from the surface. The inner zone is the solid fuel, whose thermo-physical properties are supposed constant, where the temperature decreases from T_m to the ambient, T_a , at infinite distance from the surface. A finite-rate kinetics approach is employed rather than the critical-temperature concept of most ablation models [41], which implies that material may volatilize in the interior of the liquid layer, rather than solely at the exposed surface. The axial temperature gradients are supposed negligible, and the effect of the radial convection in the liquid layer is ignored because of both the small melt layer thicknesses and low liquid vertical velocity, for which the Peclet number is on the order of 1; hence, the one-dimensional heat conduction equation through the pyrolysing liquid layer expressed in a reference frame moving with the regressing surface, in the steady state hypothesis (the liquid layer thickness is assumed constant) is:

$$\frac{d}{d\xi} \left(\lambda_l \frac{dT}{d\xi} \right) + \rho_l c_l \dot{r}_l \frac{dT}{d\xi} + \dot{Q}_p = 0 \quad (4)$$

where λ_l denotes the thermal conductivity, ρ_l the density, c_l the specific heat (all assumed temperature dependent), and \dot{Q}_p is a volumetric source term accounting for the heat of pyrolysis. \dot{r}_l is the liquid velocity relative to the regressing surface, which can be calculated with a simple mass balance across the liquid-solid interface whereby $\rho_l(v_l + \dot{r}) = \rho_s \dot{r}$, v_l being the liquid particle absolute velocity. The relative velocity is, therefore, $\dot{r}_l = \rho_l(v_l + \dot{r}) = \rho_s/\rho_l \dot{r}$.

The overall gasification occurring in depth of the reaction layer is a temperature-sensitive process modelled with a kinetic rate law following a first order Arrhenius reaction for which the energy required by the unit mass of fuel is Δh_p . The latter has been es-

timated by simplifying the real pyrolysis process assuming paraffin wax to decompose/gasify into ethylene and hydrogen (which are, thus, the gases injected in the computational domain from the wall) through the following reaction:



If Y represents the liquid paraffin mass fraction, i.e. the ratio of the local liquid paraffin to the total (liquid plus gasified) paraffin mass, the steady-state degradation process will evolve according to the equation:

$$\rho_l \dot{r}_l \frac{dY}{d\xi} = \dot{\omega}_p \quad (6)$$

in which $\dot{\omega}_p$ is the rate of production of the gas-phase per unit volume, that is:

$$\dot{\omega}_p = \rho_l B_p e^{-E_a/RT} Y \quad (7)$$

where B_p is usually referred to as frequency factor or pyrolysis reaction rate coefficient, and has the dimension of 1/s, E_a is an activation energy, and R is the universal gas constant. Thus, the volumetric energy source in Eq. (4) is of the form:

$$\dot{Q}_p = -\dot{\omega}_p \Delta h_p = -\rho_l \Delta h_p B_p e^{-E_a/RT} Y \quad (8)$$

the negative sign is present because energy is absorbed by the fuel degradation process.

The total mass of gas evolved per unit time and surface area in the reaction zone is found by integrating Eq. (7) through the liquid layer:

$$\rho_s \dot{r}_v = \int_0^h \dot{\omega}_p d\xi = \int_0^h \rho_l B_p e^{-E_a/RT} Y d\xi = \int_0^h \rho_l \frac{\rho_s}{\rho_l} \dot{r} \frac{dY}{d\xi} d\xi = \rho_s \dot{r} (1 - Y_w) \quad (9)$$

from which the ratio of the vaporization component to the total regression rate is readily correlated to the paraffin mass fraction at the wall:

$$\frac{\dot{r}_v}{\dot{r}} = 1 - Y_w \quad (10)$$

Eq. (10), indeed, represents the fact that in case the paraffin mass fraction at the wall is null ($Y_w = 0$), regression rate is entirely due to vaporization, whereas, in case all the paraffin is liquid ($Y_w = 1$), the vaporization component is zero, and the whole fuel regression occurs through liquid entrainment.

Eq. (4) applies also to the solid zone upon substitution of the relative material properties and on the condition that the source

term is null:

$$\frac{d^2T}{d\xi^2} + \frac{1}{\delta_s} \frac{dT}{d\xi} = 0 \quad (11)$$

where $\delta_s = \alpha_s/\dot{r}$ is the characteristic thermal thickness in the solid, and $\alpha_s = \lambda_s/\rho_s c_s$ is the solid thermal diffusivity. This equation can be immediately integrated with the following boundary conditions:

$$T(h) = T_m; \lim_{\xi \rightarrow \infty} T = T_a \quad (12)$$

whereby the thermal profile in the solid is obtained as follows:

$$T(\xi) = T_a + (T_m - T_a)e^{-\frac{\xi}{\delta_s}} \quad (13)$$

and, accordingly, the thermal gradient at the interface between the solid fuel and the liquid layer, from which the heat flux into the solid is calculated:

$$-\lambda_s \left(\frac{dT}{d\xi} \right)_{\xi=h} = \frac{\lambda_s}{\delta_s} (T_m - T_a) \quad (14)$$

By combining the equations discussed above, a system of two ordinary differential equations is yielded in the unknown field temperature and liquid paraffin mass fraction:

$$\begin{cases} \frac{d}{d\xi} (\lambda_l \frac{dT}{d\xi}) + \rho_s \dot{r} c_l \frac{dT}{d\xi} = \rho_l \Delta h_p B_p e^{-E_a/RT} Y \\ \frac{dY}{d\xi} = \frac{\rho_l B_p}{\rho_s \dot{r}} e^{-E_a/RT} Y \end{cases} \quad (15)$$

with the boundary conditions:

$$\xi = 0 \rightarrow \dot{q}_w = -\lambda_l \frac{\partial T}{\partial \xi} \quad (16)$$

$$\xi = h \rightarrow \begin{cases} T = T_m \\ -\lambda_l \frac{dT}{d\xi} = \frac{\lambda_s}{\delta_s} (T_m - T_a) + \rho_s L_m \dot{r} \\ Y = 1 \end{cases} \quad (17)$$

Namely, at the liquid-gas interface ($\xi = 0$) the heat exchanged to the wall, \dot{q}_w , must be equal to the heat absorbed by conduction into the fuel, and the energy transfer from the liquid to the solid ($\xi = h$) must be equal to the heat conducted into the solid from the interface plus the energy required for the phase transformation. Note that the former condition is not in contrast with Eq. (3) that is equivalent to Eq. (16) in the limit of infinite activation energy (see Appendix B).

Only three boundary conditions are needed for the integration of Eqs. (15): given the regression rate, \dot{r} , through Eq. (17) they can be integrated, with an assigned value of the liquid layer thickness, from $\xi = h$ backward to $\xi = 0$, henceforth temperature and mass fraction at the wall as well as the heat flux can be calculated. From the second of Eqs. (15), it is clear that Y is a positive function that monotonically increases from $\xi = 0$ to $\xi = h$; thus, on the one hand, there is a maximum possible value for h , which corresponds to both $Y_w = 0$ (i.e. no entrainment occurs, fuel regression is due to vaporization alone), and to the maximum heat flux \dot{q}_w and surface temperature T_w achievable with the assigned regression rate (temperature and the absolute value of its gradient are monotonically decreasing from $\xi = 0$ to $\xi = h$). On the other hand, with a given regression rate, in the limit of the liquid layer thickness $h = 0$, there is no pyrolysis, i.e. $Y_w = 1$, and the required heat flux is minimum, which is:

$$\dot{q}_w = \rho_s \dot{r} [c_s (T_m - T_a) + L_m] \quad (18)$$

Eq. (18) can be readily derived from Eq. (3) considering that the surface temperature is equal to the melting temperature, and the vaporization fraction of the regression rate is null; it, hence, expresses that the heat flux to the wall is equal to the heat conducted into the solid (first term in the square brackets) plus the heat of melting.

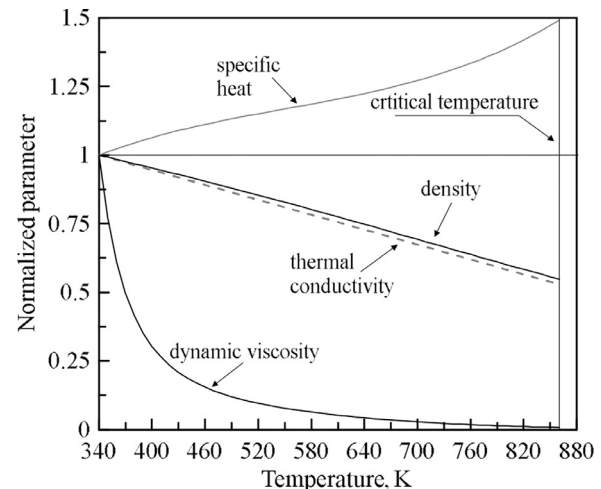


Fig. 2. Liquid paraffin thermophysical properties as a function of temperature.

However, in general h is not known, whereas the heat flux is assigned, thus an iterative procedure is required to determine the liquid layer thickness and the resulting surface mass fraction and temperature.

Paraffin-wax thermal properties as a function of temperature in the melt-layer have been estimated using the asymptotic behaviour correlations (ABCs method) reported in Ref. [33,42] with carbon number equal to 32. In Fig. 2 trends of the quantities, each normalized with respect to the corresponding value assumed at the melting temperature, are plotted in the range between melting and critical temperature; also, the dynamic viscosity is depicted because, as discussed in the next section, it appears in the liquid entrainment modelling.

The pyrolysis reaction rate constants in Eq. (7), i.e. the frequency factor B_p and the activation energy E_a , have been determined according to Ref. [43]; in particular, the former has been estimated at the average pressure in the chamber, whereas the value of the activation energy for polyethylene already used in previous simulations [24] has been selected. All the material properties are listed in Table 1.

Given the regression rate, the system of Eqs. (15) has been integrated backward with the boundary conditions in Eq. (17) by assigning the liquid layer thickness, h , by means of a fourth-order Runge-Kutta method using an adaptive step-size. The maximum value of h has been determined iteratively by imposing that the mass fraction at $\xi = 0$ was $Y_w = 0.01$ (i.e. 99% of the fuel regression is due to vaporization). The results are shown in Fig. 3.

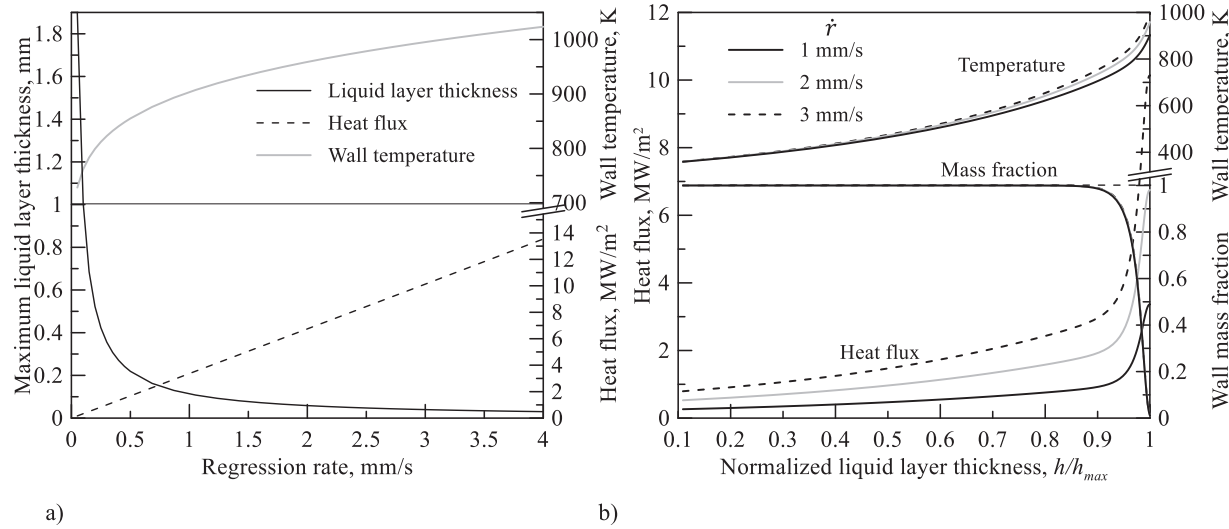
Recall that the maximum liquid-layer thickness is achieved in the absence of liquid entrainment at the surface, that is, fuel is consumed by gasification only, $\dot{r}_v/\dot{r} = 1$; with the given regression rate, in this condition the heat flux is maximum. As the regression rate increases, both the required heat flux and the surface temperature have to increase to accelerate the fuel degradation process allowing for the complete decomposition of the material into gases (Fig. 3a). The maximum liquid-layer thickness hyperbolically decreases with regression rate (Fig. 3a), as can be immediately derived considering that, as the regression rate tends to zero, approximately holds the relation (see Appendix B): $e^{-h/\delta_l} \rightarrow \text{constant}$, in which $\delta_l = \lambda_l/\rho_s c_l \dot{r}$ is the liquid-layer characteristic thermal thickness; thus, as $\dot{r} \rightarrow 0$, both δ_l and h must tend to infinity.

In Fig. 3b, heat flux, wall temperature and liquid mass fraction are reported as a function of the liquid layer thickness for three values of the total regression rate; heat flux and surface temperature both increase with the thickness and their increase is larger with larger regression rate; the three liquid layer mass fraction

Table 1

Paraffin wax properties.

Solid phase			Liquid phase (at melting temperature)				Characteristic parameters					
ρ_s , kg/m ³	c_s , J/kg K	λ_s , W/m K	ρ_l , kg/m ³	c_l , J/kg K	λ_l , W/m K	μ_l , Pa s	T_m , K	T_c , K	L_m , MJ/kg	Δh_p , MJ/kg	B_p , 1/s	E_a , kJ/mol
920	2030	0.325	780	2370	0.16	7.8·10 ⁻³	340	380	0.17	2.4	7.6·10 ⁻¹⁴	190

**Fig. 3.** a) Maximum liquid-layer thickness, heat flux and surface temperature vs. regression rate, b) heat flux, surface temperature and mass fraction vs. liquid layer thickness.

profiles are practically undistinguishable and show that the pyrolysis (also recall Eq. (10)) occurs in a portion of the layer close to the surface which is about 10% of the total thickness.

The solution of the problem in Eq. (15) and Eq.(17) has been implemented into the thermo-fluid-dynamic computations by means of a lookup table construction in order to speed up the calculations: the table has been generated in a number of total regression-rate points equally spaced of 0.1 mm/s at which Eq. (15) and Eq. (17) have been solved in 150 grid nodes in the range $h \in [0, h_{max}]$; to improve the solution accuracy close to the maximum thickness where the largest gradients are expected (see Fig. 3b), grid nodes have been spaced non-uniformly: the first node has been placed at $2 \cdot 10^{-5}$ mm far from the maximum liquid-layer thickness, and the distance between the following adjacent points increases by 5% up to $h = 0$. Given the total regression rate, each row of the table contains the following set of values: h , T_w , \dot{q}_w , \dot{r}_v/\dot{r} . The access mode to the parameters in the table is described in Sec. 2.3.

2.2.2. Liquid Entrainment Model

The rate of melt-layer entrainment at the surface, appearing in all the equations discussed above, can be estimated by means of a liquid entrainment model, which is typically based on semi-empirical correlations. The flow across the port of a liquefying fuel in a hybrid rocket can be schematised as an annular flow. The annular flow is generally characterized by a gaseous core flowing through the centre of a tube, and a liquid phase that flows partially as a thin film along the tube wall, and partially as entrained droplets dispersed in the gas phase in the centre of the tube. There is a broad spectrum of correlations developed in this framework, which have been massively investigated because of their large application in industrial processes, particularly in nuclear engineering [44]. However, the dependency of the entrainment mass transfer upon the influencing parameters has forms somewhat different from each other in the literature. Thus, a sort of pragmatic

approach is used here, which relies on identifying and resolving the most important phenomena only, while leaving second-order effects' resolution to future developments. With this view, considering that the main objective of this paper was the application of the surface-temperature calculation method addressed above, the employed liquid entrainment model is essentially the same as the one in Ref. [32], which is derived from the earlier work of Karabeyoglu et al. [7]. This latter, which strictly applies in subcritical conditions, still represents an oversimplification (with respect to the idealization of the annular flow) because it is based on the experimental results gathered in a wind tunnel where the entrainment rates from thin films of several liquids under strong gas flow were measured.

Essentially, the model predicts that the entrainment mass transfer per unit area, \dot{m}_{ent} , is proportional to the mass flow rate per unit length, \dot{m}_l , of liquid flowing on the surface (Fig. 1), basically through a function of the dynamic pressure of the gas flow ($1/2\rho_g U^2$) and surface tension, σ :

$$\dot{m}_{ent} = \rho_l \dot{r}_{ent} \propto \frac{\sqrt{\rho_g U^2}}{\sigma} \dot{m}_l \quad (19)$$

where the liquid mass flow rate was calculated in Ref. [8] by both neglecting the effect of the regression rate on the normal-to-wall velocity profile, and ignoring the variations of the fluid properties across the thickness of the liquid layer, for which the velocity profile results to be linear and, with use of the shear force balance at the liquid-gas interface:

$$\dot{m}_l = \rho_l \frac{\tau_g}{\mu_l} h^2 \quad (20)$$

in which τ_g is the mean shear stress exerted by the gas flow on the liquid surface. Upon expressing the shear stress as a function of the dynamic pressure, and getting rid of the dependency on the skin friction coefficient (which, in other words, is assumed constant), considering that the layer thickness, h , is nearly inversely propor-

tional to the total regression rate (see Fig. 2), Eq. (20) eventually leads to:

$$\dot{r}_{ent} \propto \frac{1}{\sigma} \frac{1}{\rho_g^{1.5}} \frac{G^3}{\mu_l \dot{r}^{1.5}} \quad (21)$$

where G is the total mass flux in the grain port.

In supercritical conditions, the surface tension plays a minor role and is ignored, whereby the final form of the entrainment fraction of regression rate becomes:

$$\dot{r}_{ent} = a_{ent} \frac{1}{\rho_g^{1.5}} \frac{G^3}{\mu_l \dot{r}^{1.5}} \quad (22)$$

where the constant a_{ent} is the so-called entrainment factor, which mainly depends on the physical properties of the selected fuel. Eq. (22) predicts that the tendency of a given liquefying fuel to the entrainment is roughly inversely proportional to viscosity at the characteristic temperature of the layer, and it strongly increases with the dynamic pressure of the gas. As demonstrated in Ref. [10] by means of combustion visualization techniques, the nature of the combustion process dramatically changes with increasing pressure, up to the critical pressure of the fuel. However, even in the supercritical regime, the mass transport originates from Kelvin-Helmholtz type instability, and what was proposed by Karabeyoglu et al. [7] is still the main droplet entrainment mechanism observed. The exponent of the scaling law and the parameter a_{ent} would be probably different compared to the subcritical case, but the general form of the liquid mass transfer could continue to be valid.

Here, Eq. (22) is used to calculate the local entrainment component of regression rate; it is worth remarking that in Eq. (21) the dependency of the local entrainment mass transfer on the layer thickness appearing in Eq. (20) has been replaced with that on the total regression rate, and the shear stress has been substituted with the dynamic pressure, even though both those quantities can be retrieved from the flowfield resolution. The rationale behind this choice is that, as mentioned above, the nature of entrainment depends on the structure of the rolling waves developing on the surface, which cannot be captured simply through h and τ_g , so that Eq. (22), rather than an exact punctual correlation, has to be intended as a relationship with the main influencing parameters, in which the factor a_{ent} lumps together and overshadows the local layer characteristics. In this sense, the gas density ρ_g has to be considered as the average value across the fuel grain port to account for the effect of the combustion pressure in different firings, and the mass flux as the average in the local cross section. The liquid layer viscosity is evaluated at the effective temperature of the melt layer, which is somewhere between the melting temperature and the surface temperature; it was evaluated as a weighted average of the melting and surface temperatures as suggested in Ref. [43]: $(T_w + 2T_m)/3$.

2.2.3. Boundary Conditions at the Fuel Surface and Solution Strategy

The variables needed at the fuel surface are the velocity components, temperature, mixture fraction, turbulent kinetic energy and dissipation rate. In the following, the procedure used for the relative assignment is addressed. The fuel mass fluxes associated to the vaporization and entrainment components, respectively, are obtained as follows

$$\dot{m}_v = \rho_s \dot{r}_v \quad (23)$$

$$\dot{m}_{ent} = \rho_s \dot{r}_{ent} \quad (24)$$

The vaporization and entrainment components of regression rate are handled differently for a correct evaluation of the blocking effect of the heat transfer to the surface. The vaporization component is treated in the same means as in the case of a classical

pyrolyzing fuel, considering the mass and mixture-fraction balance equations at the grain wall, given by, respectively:

$$(\rho v)_w = \dot{m}_v \quad (25)$$

$$(\rho v)_w f_w + \left(\frac{\mu_t}{Sc_t} \frac{\partial f}{\partial \xi} \right)_w = \dot{m}_v \quad (26)$$

where f is the mixture fraction, ρ is the gas density, and v is the normal-to-wall velocity component generated by the gaseous products injection, both of them evaluated at the wall; μ_t and Sc_t are the turbulent viscosity and turbulent Schmidt number, respectively (for the hypothesis of unity Lewis number, the turbulent Schmidt number is equal to the turbulent Prandtl number and they are fixed to 0.85). Eq. (26) simply states that the mass flux of gassified fuel entering the computational domain as a consequence of the relative regression rate fraction (which appears on the right-hand side of the equation and represents a production term) is partially balanced by convection and partially by diffusion of the fuel mass fraction f . Although the actual products of fuel pyrolysis are numerous and their composition depends on both the wall temperature and heating rate, here gaseous ethylene and hydrogen as stated in Eq. (5) are injected from the surface. The entrained liquid fuel does not contribute to the heat transfer blocking, then the resulting mass flux is not introduced into the combustion chamber from the grain wall. In fact, as a single-phase approach is used in this study on the simplifying assumption that, being the entrained paraffin in the supercritical state, it is immediately gasified for the rapid turbulent mixing and large combustion heat release, the local entrainment contribution is uniformly assigned, as a mass production term of both the mass and mean mixture fraction balance equations (S_m in Appendix A), in the local volume of the grain port corresponding to the surface cell through which the fuel mass enters the fluid domain. The energy required by the pyrolysis of the liquid fuel mass flow rate is taken into account by assigning in the same volume a corresponding negative energy source term (S_h in Appendix A).

Balance of the mixture-fraction variance at the wall is ignored, and it is imposed to be zero. The no-slip boundary condition is enforced for the parallel-to-wall velocity component. The required level of mesh refinement near the grain surface allows for the resolution of the viscous sub-layer, so that the boundary condition for the turbulent kinetic energy is assigned enforcing null normal gradient at the surface, whereas the specific dissipation rate is imposed as suggested in the Menter's standard model for smooth walls [35].

The overall solution procedure is approached through the following steps.

- 1) Input the boundary conditions and a combustion pressure reference value; at the grain surface trial values of the unknown required temperature, regression-rate vaporization component and mixture fraction are used. Furthermore, a total regression rate is also assigned.
- 2) Computation of the thermodynamic lookup table containing the time-averaged values of species mass fractions, density, and temperature as a function of mean mixture fraction, mixture fraction variance, and enthalpy.
- 3) Solution of the mass, momentum, turbulence and mixture fraction equations.
- 4) Calculation of the spatial distribution of temperature, density and individual chemical species mass fractions by interpolating the values in the thermodynamic lookup table.
- 5) Scaling of the density field with pressure with respect to the reference value (dependence of temperature and mixture composition on pressure is neglected).

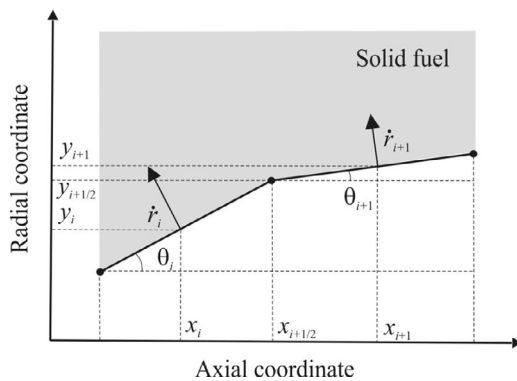


Fig. 4. Schematic representation of the port geometry update.

- 6) From the results of the simulation, the convective heat flux to the wall is evaluated, thereby, from the lookup table (with the wall heat flux and total regression rate) the new wall temperature, vaporization regression rate is extracted through a bilinear interpolation, and Eqs. (22), (25) and (26) are solved simultaneously to compute the new distribution of the variables along the grain surface and, accordingly, the mass flux distribution along with the volume source terms.

Steps from 3) through 6) are, then, iterated by adjusting the local values of the mentioned quantities until convergence is reached.

2.3. Transient solution procedure

For a better estimate of the regression rate, as will be discussed later, other than single simulations carried out at the port diameter averaged over the space and burning time, transient, quasi-steady state calculations have been performed. Considering that the fluid dynamic characteristic time is much shorter than the time required for the thermal profile adjustment in the solid grain due to a change in the port diameter, a series of steady state simulations are carried out in a number of time steps in which the burning duration is split.

Once the regression rate at the middle of the face of each boundary cell is computed, the local port geometry is updated through the local node displacement calculation following a Euler explicit time integration scheme with time-step amplitude Δt :

$$\Delta_i^n = \dot{r}_i^n(x_i)\Delta t \quad (27)$$

where Δ_i^n is the i th face displacement, and \dot{r}_i^n is the regression rate both evaluated at the n th time step. The procedure used for the nodal displacement decomposition is shown in Fig. 4: the regression rate is, by definition, normal to the fuel surface, therefore the local vector displacement includes both axial and radial components.

Denoting with θ_i^n the local inclination of the i th cell face on fuel surface with respect to the axial direction, the coordinates of the face centre at the $n+1$ time step is:

$$x_i^{n+1} = x_i^n - \Delta_i^n \sin \theta_i^n \quad (28)$$

$$y_i^{n+1} = y_i^n + \Delta_i^n \cos \theta_i^n \quad (29)$$

from which the displacement of the node $i+1/2$ in between two consecutive cells is calculated by interpolation and the updated local port diameter is, of course, $D_{i+1/2}^{n+1} = D_{i+1/2}^n + 2\Delta y_{i+1/2}^n$. The fluid domain geometry is modified accordingly, and a new computational mesh is generated; a steady-state numerical simulation at the new time step $n+1$ is, then, performed.

3. Numerical results and model validation

Results obtained with the computational model combined with the novel technique for the liquefying fuel regression treatment described above are shown in this section. First, a number of experimental test cases are presented, which are used in the following for a comparison with the computational results. Secondly, the sensitivity of the numerical results to the grid size is examined; finally, the capability of reproducing the experimental data with the steady and transient solutions is discussed.

3.1. Experimental test cases and comparison with numerical results

A series of static firing tests of a laboratory-scale hybrid rocket in the 200-N thrust class burning paraffin-based fuel grains, made of a blending of a low-melting point paraffin wax and a micro-crystalline wax, with gaseous oxygen are selected as test cases. The rocket layout is shown in Fig. 5; the axisymmetric combustion chamber is 350 mm long and has 69-mm inner diameter. Upstream and downstream of the solid grain a dump plenum and an aft-mixing chamber are set up, respectively, where pressure is measured. Oxygen is axially injected through a converging conical nozzle with 6-mm exit diameter in the grain single port; injected mass flow rate is measured through a choked calibrated venturi. Such an injector accelerates the oxygen jet emerging from the lip and generates a recirculation region in the port front, which, as already widely examined, favours the propellant mixing and promotes both higher combustion efficiency [45] and better stability [46]. The rocket was equipped with a graphite converging-diverging exhaust nozzle.

Further details of the experimental test rig can be found in Ref. [16]. A subset of five test cases, which were considered in the previous authors' work [32,18], is retained here: the first two tests included in Ref. [32] are excluded as the condition of supercritical pressure regime in the combustion chamber is not met. The average (either time or time-space averaged) parameters measured in the firings are listed in Table 2 with the relative measurement uncertainties. The mass loss method [47] has been applied to calculate the average values starting from the measurement of the consumed fuel mass, ΔM , and burning time; the average final port diameter, D_2 , is obtained as follows:

$$D_2 = \sqrt{D_0^2 + \frac{4}{\pi} \frac{\Delta M}{\rho_s L}} \quad (30)$$

from which the average port diameter is $D_{ave} = 0.5(D_2 + D_0)$, and, accordingly, the time and space-average regression rate:

$$\dot{r}_{ave} = \frac{D_2 - D_0}{2t_b} \quad (31)$$

where t_b is the effective burning time that is determined from the pressure-time trace as the period from the inflection point on the first main rise portion of the prechamber pressure signal and the one on the decrease phase. The local time average regression rate is obtained by sectioning the fuel grains after the firing in a number of slices and measuring the local web thickness, from which the port diameter $\hat{D}_2(x_i)$ at the local axial coordinate is calculated, and the corresponding regression rate:

$$\hat{r}(x_i) = \frac{\hat{D}_2(x_i) - D_0}{2t_b} \quad (32)$$

The engine extinguishment is realized by closing the oxygen valve and immediately purging nitrogen in the combustion chamber. This procedure insures that combustion is stopped exactly when the valve is closed, but may have an effect on the regression rate measurement accuracy, which is hard to be assessed. In fact, in particular in the fuel grain fore region, the experimental

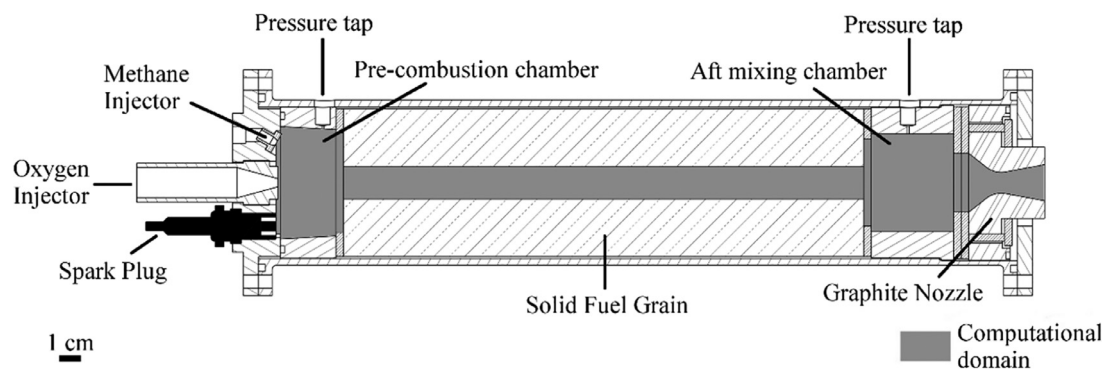
**Fig. 5.** 200-N scale laboratory-hybrid rocket layout.

Table 2
Average operating parameters measured in the firing tests.

Test ID	Initial port diameter, mm	Oxidizer mass flow rate, g/s	Grain port diameter, mm	Oxidizer mass flux, kg/m ² s	Regression rate, mm/s	Overall mixture ratio, O/F	Chamber pressure, bar
3	15	38.0 ± 0.85	26.6 ± 0.16	67.83 ± 2.30	2.04 ± 0.13	1.10 ± 0.09	11.2 ± 0.011
4(*)	15	42.0 ± 1.35	27.1 ± 0.10	72.58 ± 2.83	2.29 ± 0.15	1.08 ± 0.10	12.9 ± 0.013
5	20	55.5 ± 1.36	29.0 ± 0.04	83.75 ± 2.26	2.41 ± 0.17	1.26 ± 0.11	16.9 ± 0.017
6	15	59.5 ± 1.66	28.0 ± 0.12	96.76 ± 3.48	2.73 ± 0.20	1.19 ± 0.10	18.4 ± 0.018
7	15	60.5 ± 1.56	27.1 ± 0.10	105.22 ± 3.50	2.96 ± 0.23	1.20 ± 0.11	19.1 ± 0.019

(*) Reference test for the grid sensitivity analysis.

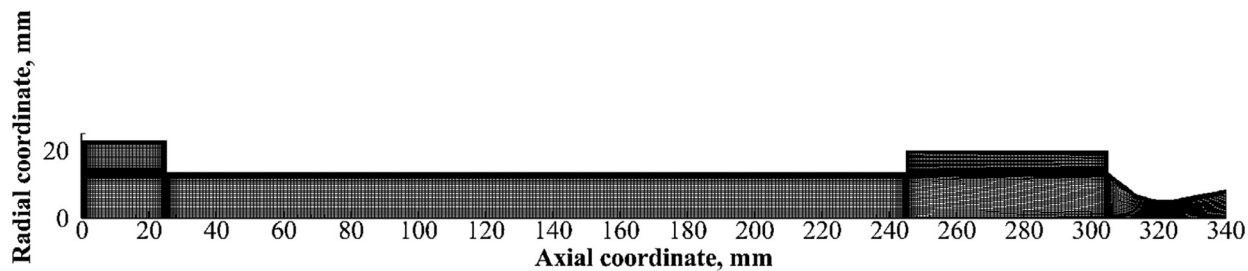
**Fig. 6.** Reference computational grid.

Table 3
Computational domain dimensions (Test 4).

Prechamber diameter	Prechamber length	Fuel grain length	Fuel grain port diameter	Postchamber diameter	Postchamber length
46 mm	25 mm	220 mm	27 mm	40 mm	60 mm

uncertainty is expected to be larger because of the unburned recirculated melted paraffin that is deposited on the grain surface after the motor extinguishment by means of the high-pressure nitrogen flow.

The main purpose of the experimental campaign was to measure the average regression rate obtained by varying the average oxidizer mass flux, which was realized with two initial port diameters of 15 and 20 mm and different oxygen mass flow rates, keeping the burning duration nearly constant to around 5 seconds.

The whole computational domain includes the internal volume of the prechamber, the fuel grain, the postchamber and the nozzle, as sketched in Fig. 5 and Fig. 6 in which the numerical grid relative to the geometry of the grain port of Test 4 (with average port diameter) is depicted. The main dimensions are listed in Table 3. No-slip and adiabatic boundary conditions are imposed on the inner surface of both the prechamber and postchamber as well as on the nozzle wall. A mass flow rate and total temperature boundary condition are enforced at the injector outlet section with the oxygen mass fraction and the turbulent quantities assuming fully developed flow. A pressure outlet condition is set at the nozzle exit section.

The reference grid is made by 40×80 cells in the axial and radial directions, respectively, in the prechamber; the grain port is subdivided in 240×40 grid cells, the postchamber in 80×80 cells and the nozzle in 60×40 cells. Cells are clustered towards the grain wall to ensure that the value of y^+ is lower than 3 in all the wall-adjacent cells. Additional axial clustering of cells is placed in the regions near the grain inlet and outlet edges, and near the prechamber, postchamber and nozzle inner surfaces. With reference to Test 4, a grid sensitivity analysis was carried out with three mesh refinement levels to determine the dependence of numerical results on the spatial discretization. A coarser and a finer mesh are constructed starting from the reference mesh: they are generated respectively doubling and halving the cell size in both the axial and the radial directions (in the clustering zone the size is set only for the first layer, while the size of the subsequent layer depends on the bunching law). Fig. 7 shows a log-log plot of the numerical error versus the minimum grid size for the average values of the total regression rate and the grain surface temperature.

The numerical error is calculated as the relative difference between the value obtained in the simulations (which are resumed in Table 4) and the relevant Richardson's extrapolation. A maxi-

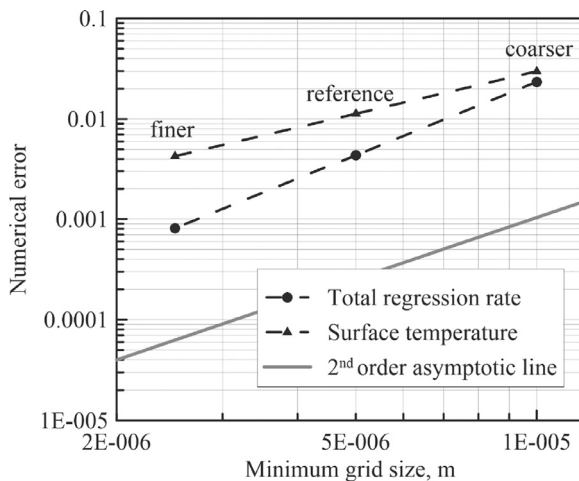


Fig. 7. Numerical error versus grid size.

Table 4
Grid sensitivity analysis results (Test 4).

Mesh refinement	Total regression rate, mm/s	Surface Temperature, K
Coarser	2.307	760
Reference	2.268	774.5
Finer	2.262	780

mum deviation of 2.5% with respect to the finer mesh is calculated for the surface temperature. The total regression-rate deviations are less than 2%. Therefore, a satisfactory approximation of the numerical results is believed to be obtained with the reference mesh.

3.1.1. Effect of oxygen mass flux

The influence of the oxygen mass flux on the flowfield and the parameters derived at the fuel surface is analysed by taking Test 4 as a reference, maintaining the port diameter constant to the average value of 27 mm measured in the experimental test, and varying the oxygen mass flow rate. For the evaluation of the entrainment fraction of regression rate, the entrainment parameter, a_{ent} , has been calculated, as a first trial, by scaling the value of $2.1 \times 10^{-13} \text{ m}^{8.5} \text{s}^{0.5} / \text{kg}^3$, which was identified in Ref. [32] for the best fit with the measured average regression rate of Test 4. Note, that value lumped the constant entrainment factor defined here with the average gas density calculated in Test 4 ($\rho_g^* = 1.58 \text{ kg/m}^3$) and the constant liquid viscosity; thus, with multiplying by the proper density and viscosity (evaluated at the surface temperature equal to 675 K), the first-guess scaled parameter was $a_{ent} = 5.44 \times 10^{-16} \text{ m}^3/\text{s}^{0.5} \text{ kg}^{0.5}$, which resulted in a regression rate too large compared to the experimentally measured one. Finally, with decreasing the factor by 25% (i.e. by the ratio of the liquid viscosity at the calculated average surface temperature to that at 675 K) allowed matching the measured total regression rate with tolerance less than 1%; in conclusion, the derived constant in Eq. (22) is $a_{ent} = 4.0 \times 10^{-16} \text{ m}^3/\text{s}^{0.5} \text{ kg}^{0.5}$. The variation of the gas density in the combustion port from one test case to another, as predicted by Eq. (22), has non-negligible effect, accordingly the entrainment regression rate is adjusted by scaling with the ratio $(\rho_g^*/\rho_g)^{1.5}$.

First, a comparison with the results obtained with the constant surface-temperature model [32] is drawn for Test 4. In Fig. 8 the axial profiles of regression rates as well as of wall heat fluxes are contrasted with each other, and in Table 5 the corresponding average values are listed. The average total regression rates calculated with the two models are practically equal and in excellent agree-

ment with that measured, yielding a deviation of around 1% (for further details see Sec. 3.1.2). The constant surface temperature estimated with the previous model is much lower than that calculated with the current one, which predicts an average value about 100 K larger; whereas, the relative vaporization fraction of regression rate is larger except in the port outlet region where it is null (Fig. 8a).

In fact, in the previous model, the vaporization regression rate was imposed equal to zero when the entrainment component computed with the counterpart of Eq. (22) exceeded the total regression rate resulting from the energy balance in Eq. (3), so that the total regression was entirely generated by entrainment. Note that in the current model this unphysical behaviour is overcome as the vaporization component is associated to variable surface temperature. The regression rate entrainment component continuously increases along the grain port because of the dependence on the total mass flux and the values calculated with both models are nearly equal as expected from the mild variation of the liquid layer viscosity with temperature. As a result, the total regression rate curves are approximately overlapped except in the outlet region where the two vaporization fractions are significantly different. According to what pointed out above, by increasing the surface temperature, the regression rate is decreased.

Fig. 8b shows the computed wall heat fluxes; both are monotonically increasing down the port and tend to flatten in the zone around 30–60 mm, which, as discussed in the forthcoming paragraphs, is due to the gas recirculation in the port entrance. The heat flux, indeed, would tend to achieve a maximum point in the neighbourhood of the oxygen jet impingement point on the fuel surface (as shown in Ref. [24] dealing with classical non-liquefying fuel with slower regression), but, for the intense mass addition from the wall and the resulting growth of mass flux, it continuously increases. Overall, the previous model predicts larger heat flux for the lower surface temperature; the difference increases in the outlet region where the vaporization is null for the consequent disappearance of the blowing effect.

The results obtained with four different values of the oxygen mass flow rate (three more than that relative to Test 4 itself) are shown in Fig. 9 in terms of total temperature contours, streamlines (depicted on the top half of the pictures) and fuel mass fraction isolines (on the bottom half).

At the motor head end the typical recirculation region induced by the interaction of the oxygen discharged from the converging nozzle injector and the solid grain wall can be clearly seen. The details of the flowfield in the prechamber and fuel grain entrance region are shown in Fig. 10, where the oxidizer mass fraction ($1-f$) and turbulence intensity contour maps are plotted on the top half and on the bottom half of the picture, respectively. Values of the turbulence intensity map are normalized with respect to the local maximum intensity in the depicted region.

The core of the oxygen jet issued by the nozzle injector is visible from both the velocity vectors and the nearly unity oxygen mass-fraction area; as expected, the velocity radial profiles lose the flat shape yielded immediately downstream of the injector exit section and show the characteristic Gaussian-type shape. The edge of the jet can be recognised from the largest turbulence level achieved in the field, which occurs at the position of maximum shear, whereas at the centreline, where the shear tends to zero, turbulence strength is much less. The calculated jet spreading angle is around 10 deg, which is close to the one characteristic of a free jet [48]. The extension of the flow recirculation (which is decided by the oxygen jet spreading) is practically independent from the mass flux in the port, it being confined up to around 60 mm downstream of the injection flange in all the four test cases analysed. With given prechamber length, the main parameter affecting the extension of the recirculation in the port is, indeed, the grain

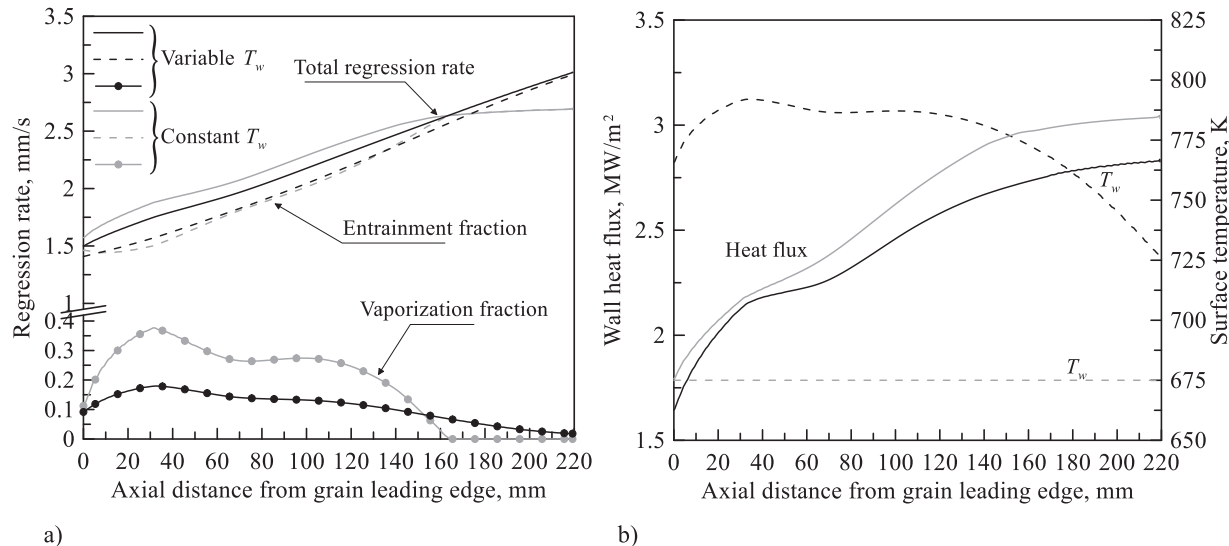


Fig. 8. Comparison between the results obtained considering constant or variable surface temperature: a) regression rate, b) surface temperature and wall heat flux.

Table 5
Average surface parameters calculated with variable and constant surface temperature models.

Model		
	Variable surface temperature	Constant surface temperature
Surface temperature, K	778	675
Wall heat flux, MW/m ²	2.45	2.61
Total regression rate, mm/s	2.27	2.27
Vaporization component, mm/s	0.10	0.19
Entrainment component, mm/s	2.16	2.08

port diameter, which determines the oxygen jet impingement point on the fuel surface [49]. Note that, thanks to the main vortex ring at the entrance of the fuel port, fuel is transported back to the periphery of the prechamber where two other vortex structures contribute to mixing with the oxidizer from the jet core; the resulting local mixture ratio is equal to about 1 entailing high temperature in the prechamber also.

Whereas, by increasing the oxygen mass flow rate, the momentum of the oxygen jet increases and the cold-flow core on the port centreline tends to penetrate farther downstream along the grain. This aspect can be clearly seen from the temperature radial profiles traced at the grain inlet ($x = 25$ mm in Fig. 9), middle ($x = 135$ mm) and outlet ($x = 245$ mm) sections in Fig. 11. In the inlet section, the average temperature reached with the four mass fluxes does not show significant changes, yielding a maximum at about half of the port radius. In the same section, the size of the jet core is practically unaltered, there is no mixing with the fuel, and the temperature is equal to the one at the injector outlet all over its exit section radius (6 mm / 27 mm = 0.22). In the middle section, temperature is on average larger owing to more efficient mixing of propellants, and the maximum point shifts closer to the fuel surface; interestingly, with the lowest mass flux (oxygen mass flow rate equal to 10 g/s), in the grain middle section, the oxygen-to-fuel mixture ratio is close to the stoichiometric one (the stoichiometric mass fraction value is around 0.23, see Fig. 9a) from the port centre to about half of the section. In the outlet section, the case yielding the largest temperature is that with the largest mass flux, whereas the lowest mass flux case shows the lowest temperature.

In all the four cases the total regression rate increases down the port almost linearly (see Fig. 12a), and higher is the oxygen mass flux, larger is the growth. In fact, as the vaporization fraction

is less than 10% (Fig. 8b), it can be neglected in Eq. (1), and from Eq. (22) it can be readily derived that the regression rate roughly depends on the total mass flux raised to the power of 1.2. Hence, by means of integration of the mass balance equation in the pot, $dG = 4\rho_s \dot{r} dx/D$, the local total mass flux is determined, hence one obtains [50]:

$$\dot{r} = a G_{\text{ox}}^{1.2} \left(1 - 0.8 \frac{a \rho_s}{D} G_{\text{ox}}^{0.2} x \right)^{-6} \quad (33)$$

in which the coefficient $a = (a_{\text{ent}}/\rho_g^{1.5} \bar{\mu}_l)^{0.4}$, and $\bar{\mu}_l$ is the average value of the liquid viscosity on the fuel surface; by expanding Eq. (33) in series up to the first order, the following regression-rate approximate expression is immediately derived:

$$\dot{r} \cong a G_{\text{ox}}^{1.2} \left(1 + 4.8 \frac{a \rho_s}{D} G_{\text{ox}}^{0.2} x \right) \quad (34)$$

which, being the term $0.8a\rho_s L/DG_{\text{ox}}^{0.2}$ nearly equal to 0.5, explains the axial trends in Fig. 12a.

The vaporization regression rate, as expected, grows with the oxygen mass flux, and the axial trends show maximum points about 35 mm downstream of the inlet (which is more evident from Fig. 12b where the vaporization-to-total regression rate ratio is depicted), i.e. where the oxygen jet impinges on the fuel wall and, as remarked above, the heat flux tends to flatten (Fig. 8b); the surface temperature displays similar axial profiles.

Interestingly, despite the different axial profiles, the peak value achieved by the ratio \dot{r}_v/\dot{r} over the port length is nearly equal to 0.1 regardless of the mass flux, whereas the average ratio increases with the mass flux itself.

Eq. (33) can be analytically integrated over the port length to calculate the space averaged regression rate, \dot{r}_L , to give:

$$\dot{r}_L = 0.25 \frac{D}{L} \frac{G_{\text{ox}}}{\rho_s} \left[\left(1 - 0.8a \rho_s \frac{L}{D} G_{\text{ox}}^{0.2} \right)^{-5} - 1 \right] \quad (35)$$

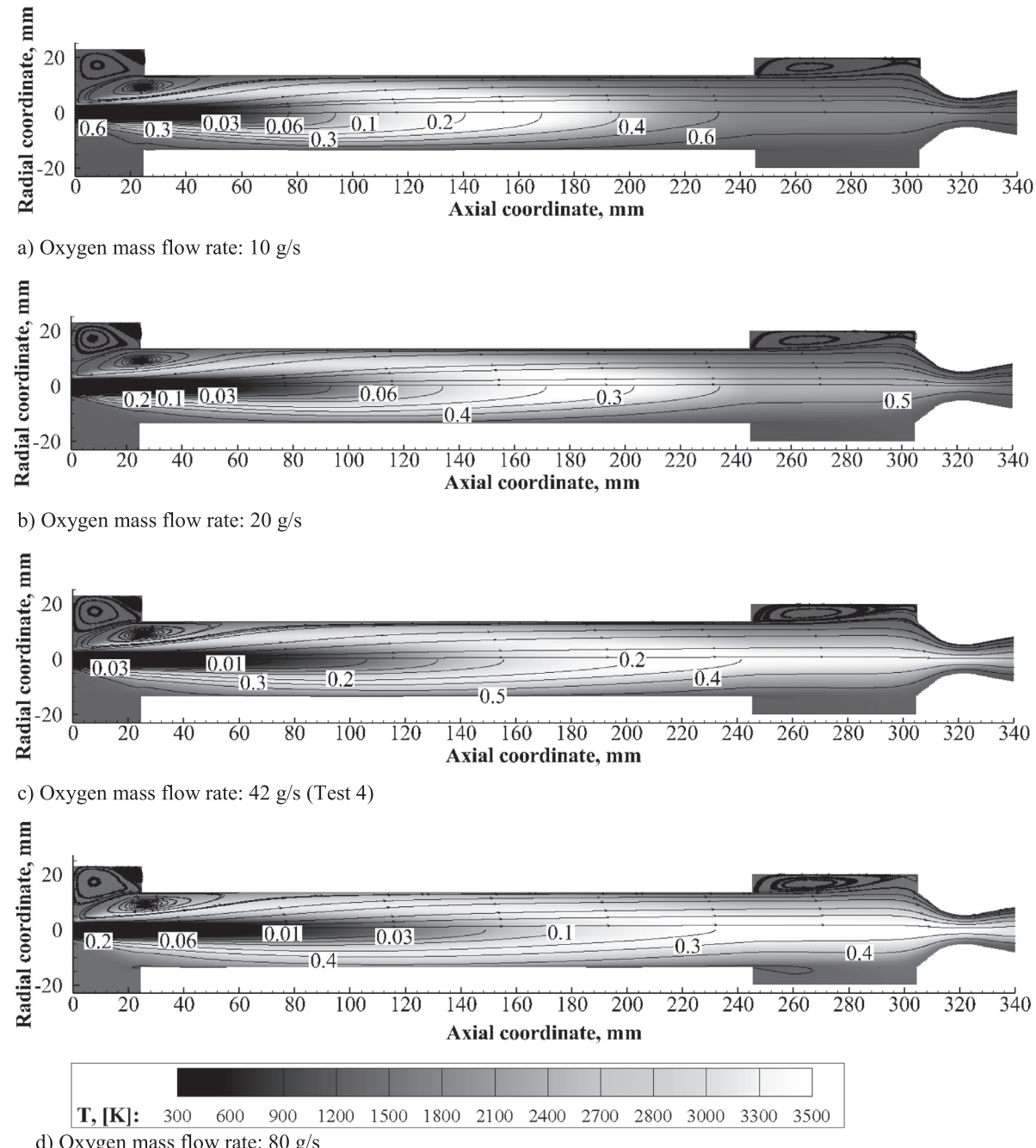


Fig. 9. Total temperature contours plot with overlapped streamlines (top half) and mixture-fraction isolines (bottom half).

A comparison between the results obtained with Eq. (35) and the exact values derived from the CFD simulations is shown in Fig. 13 (where one more case at 30 g/s oxygen mass flow rate is included).

It is clear that Eq. (35) underestimates the regression rate, as expected because of the vaporization component drop in Eq. (22). The underestimation is, indeed, higher with larger mass flux as the latter entails larger vaporization; however, in the analysed conditions, it is lower than 5%.

3.1.2. Rebuilding of the experimental data

Numerical simulations were carried out in the conditions of oxygen mass flow rate and average port diameter of the firing tests in Table 2 with the constant value of the entrainment parameter derived above; the results in terms of the calculated average re-

gression rate are listed in Table 6 with the relative deviations from the experimental data. The calculated regression rates are biased to values all lower than the experimental ones, which can be adjusted by properly increasing the entrainment factor. However, the maximum error is 4.5%, which was believed acceptable in order to demonstrate the model capability.

By cross-checking the average port diameters in Table 2 and the corresponding regression-rate percent deviations in Table 6, a correlation between the port diameter and the magnitude of the deviation from the experimental data seems to be likely: with larger port diameter, the calculated regression rate tends to be increasingly lower than the measured one. This tendency was somewhat expected and is supposed to be produced by the effect of the recirculation region at the port inlet that grows with the port diameter. The employed entrainment model, indeed, neglects the skin fric-

Table 6
Computed regression rate deviations from experimental data.

Test ID	Calculated space-averaged regression rate, mm/s	Error relative to experimental data
3	2.04	-0.15%
4	2.27	-0.9%
5	2.30	-4.5%
6	2.62	-4.1%
7	2.85	-3.4%

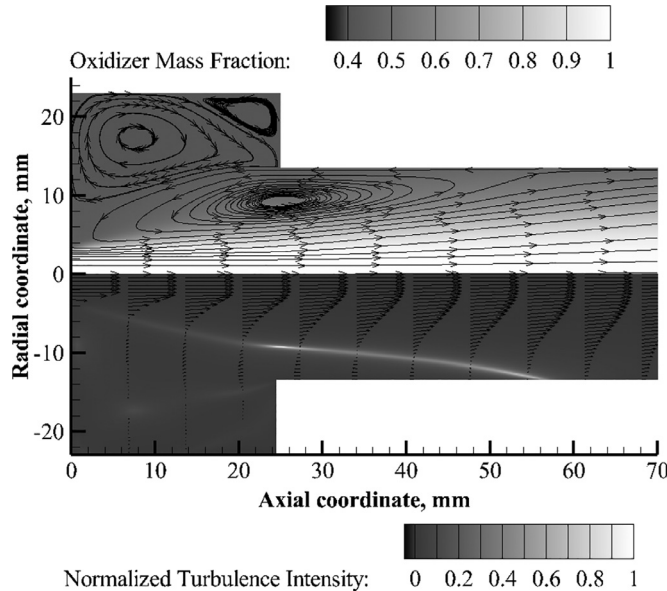


Fig. 10. Detail of the flowfield at the motor head and (Test 4).

tion variation and, thus, is not able to capture adequately the mass transfer phenomenon in the presence of recirculation. Recall that with 27-mm diameter, the recirculation is confined into the fore 10% of the port length.

Test points are plotted as a function of the oxygen mass flux in Fig. 14 along with the data calculated at the constant port diameter of 27 mm presented above. Test data follow the same trend displayed by the total regression rate calculated at constant diameter, which yields a dependency on the oxygen mass

flux in the form of a power with the exponent equal to about 0.6. By expanding Eq. (35) in series, the average regression rate can be approximated to $\dot{r}_L = aG_{ox}^{1.2}$, in which the factor a actually depends on the mass flux through the average gas density in the port, which increases with the latter, implying a regression-rate variation with the mass flux lower than what explicitly appears in Eq. (35). It is worth remarking that also the calculated regression rate vaporization component increases with a mass-flux power, but yielding 0.8 exponent. This larger exponent is equal to that predicted by the classical turbulent boundary-layer diffusion limited regression rate model [13], and confirms that the surface vaporization is mostly dictated by the heat transfer to the wall.

On the same diagram five test points from the literature are overlapped [51]. They were retrieved from ground firing a smaller hybrid rocket burning gaseous oxygen with a microcrystalline-wax based fuel with 100 mm grain length and 40 mm initial port diameter, under lower mass fluxes. The measured regression rates are larger than those measured in Naples by nearly 25%, but seem to show the same trend (equal slope on the mass flux basis). The reason can be inferred considering that tests in Ref. [51] were conducted at substantially lower chamber pressure (in the range 3 - 7.4 bar) for which wax is below, or close to, the critical pressure regime, and the gas density in the port is also lower than that obtained in the current tests; according to Eq. (35), at equal mass flux, regression rate is, therefore, expected to be larger. To support this hypothesis, in all the tests (i.e. both current ones and those in Ref. [51]) regression rate has been calculated with Eq. (35) in which the gas density has been estimated from the measured propellant mixture ratio and pressure in thermochemical equilibrium conditions [40]. Fuel surface temperature has been assumed equal to 700 K for tests in Ref. [51] based on the arguments in Ref. [43]. The entrainment factor (which essentially depends on the fuel properties) has been

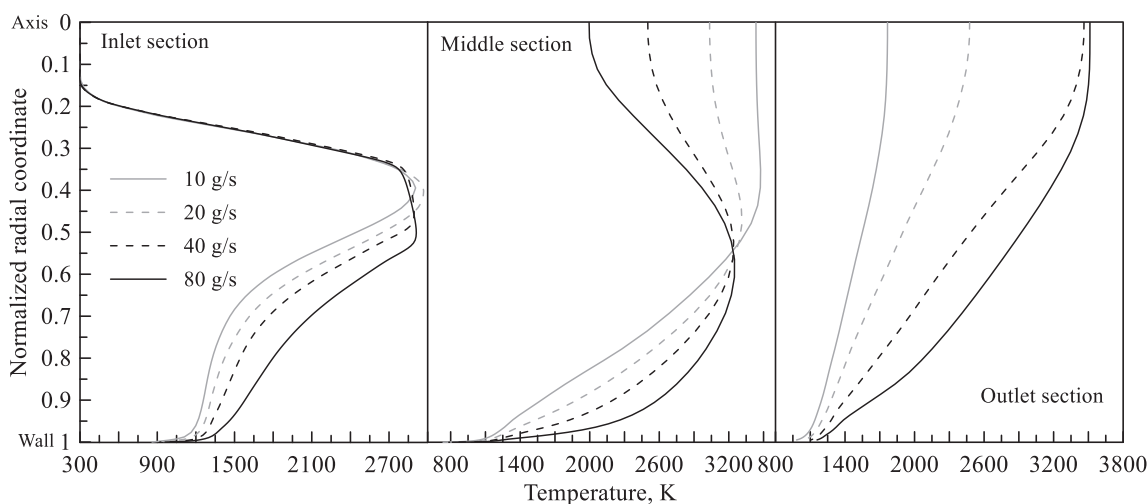


Fig. 11. Total temperature radial profiles in the grain inlet, middle and outlet section.

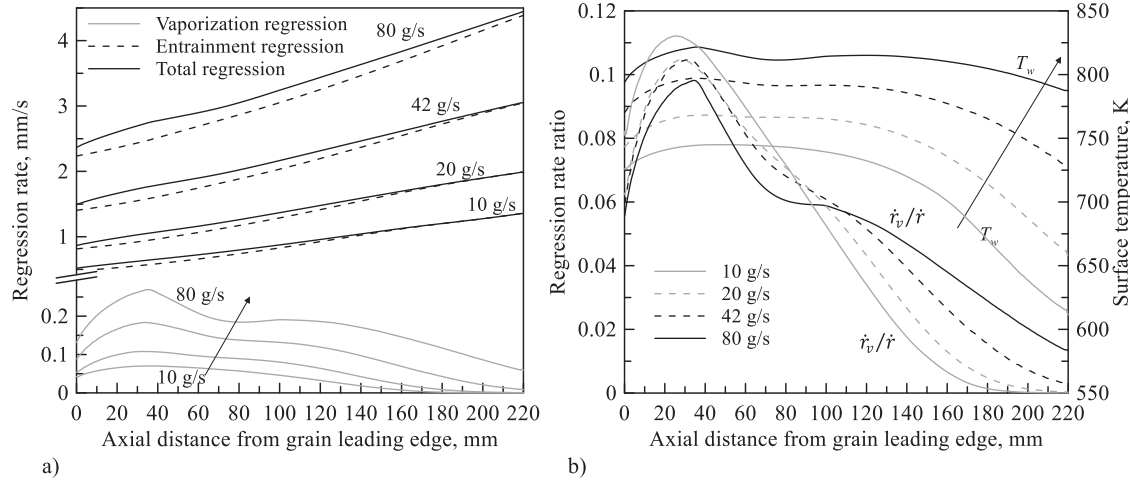


Fig. 12. Axial distribution of fuel surface parameters: a) regression rate components, b) vaporization-to-total regression rate ratio and surface temperature.

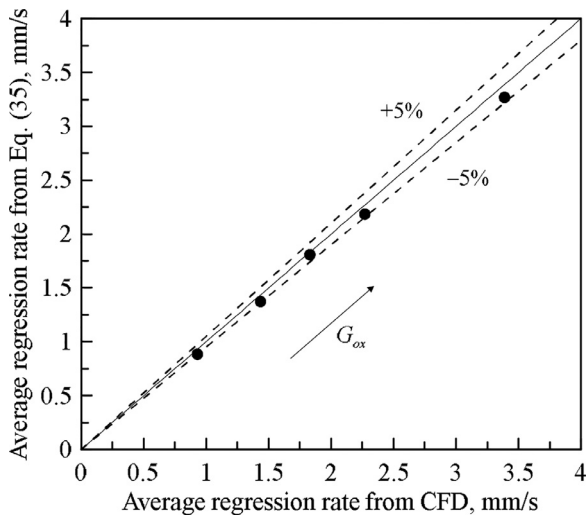


Fig. 13. Space-average regression rate error.

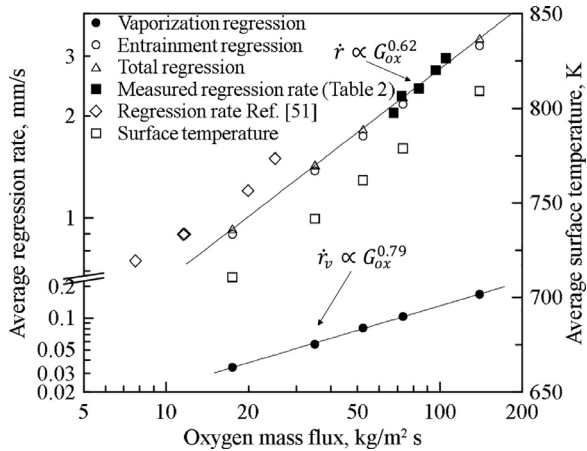


Fig. 14. Average regression rates and surface temperature vs. oxygen mass flux.

kept equal to that used in the CFD simulations presented here. Results are shown in Fig. 15; the agreement between the estimated and measured regression rates is fair in all the cases being within $\pm 10\%$, which gives a reasonable basis to the observation advanced above.

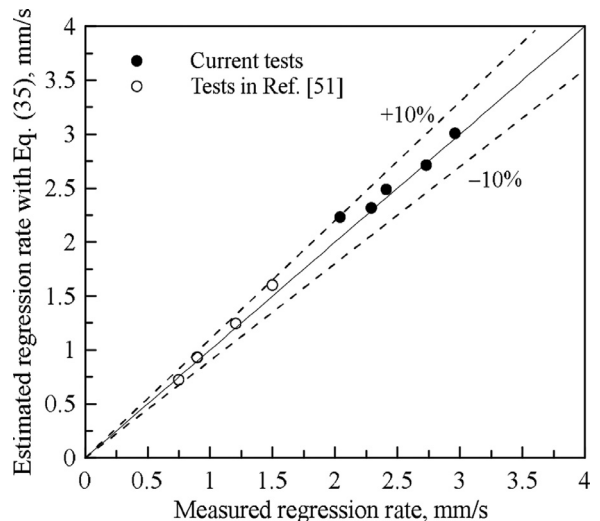


Fig. 15. Average regression rate estimated with Eq. (35).

3.1.3. Transient solution results

As shown in the previous sections, the presented computational model is quite able to predict the average regression rate achieved in a rocket firing experiment by carrying out CFD simulations at the grain port diameter averaged in space and time; nevertheless, it fails to capture the time averaged regression rate axial profile as can be clearly derived from Fig. 16 by comparing the dashed line (see also Fig. 12a) with the black points. Though the average value is fairly well calculated, regression rate is underestimated in the grain inlet and overestimated in the outlet portion.

The reason may be that, as the liquid entrainment is the main regression rate driver and being it strongly affected by the mass flux, with a given regression rate the local diameter plays a major role in the mass flux determination. The port diameter averaged over the firing time and grain length is, of course, larger than the time averaged local diameter measured in the inlet section, whereas it is lower in the exit. Thus, considering the proper diameter for the mass flux evaluation should compensate for the observed disagreement. A transient numerical simulation has been carried out in the conditions of Test 4 according to the procedure described in Sec. 2.4; the initial port diameter is 15 mm and the firing duration is 5.2 s. Advancement in time has been carried out with a variable time step to reduce the explicit time integration er-

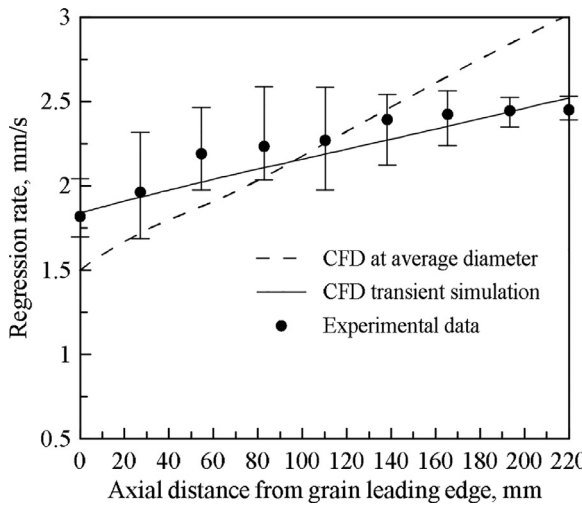


Fig. 16. Comparison between numerical results and experimental data of average regression rate axial profile in Test 4.

ror: over the first 1-s burning period, when the regression rate is the largest, the selected time step was 0.1 s, after that, increasingly longer time steps were adopted.

Starting from the initial time instants, for the non-negligible port enlargement over time, the characteristics of the thermo-

fluid-dynamic field significantly change. In fact, on the engine ignition, the oxygen jet definitely remains outside of the port, as can be observed in Fig. 17a where the flow recirculation is clearly seen to be located only in the prechamber. As the port opens up, the oxygen jet impingement point on the fuel surface moves downstream and the jet core penetrates farther along the port. The hottest region in the flow shifts to the right with time as the fuel consumption rate slightly decreases ($\dot{m}_f \propto \dot{m}_{ox}^{1.2} D^{-0.24}$), and the stoichiometric oxidizer to fuel ratio is reached further downstream. This configuration causes different distributions of the heat transfer to the wall and fuel vaporization rates.

The port diameter axial profiles calculated in a number of time instants in the burn are depicted in Fig. 18. Each profile approximately shows a linear trend whose slope tends to increase with time (i.e. with the port diameter) as predicted by the approximate relationship in Eq. (34) and the arguments addressed above. The calculated port shape at the end of the burn is compared with the one measured in Fig. 18; an analogous comparison is drawn in Fig. 16 in terms of regression rate. The fuel axial consumption profile obtained with the transient simulation is overwhelmingly more accurate than the corresponding estimate provided by the calculations at the average diameter; the maximum deviation of the calculated diameter from the measured one is about -8% (which is well within the experimental uncertainty) and is observed at 55 mm downstream of the grain inlet section where the flow recirculation is expected to have non-negligible influence (see Fig. 17).

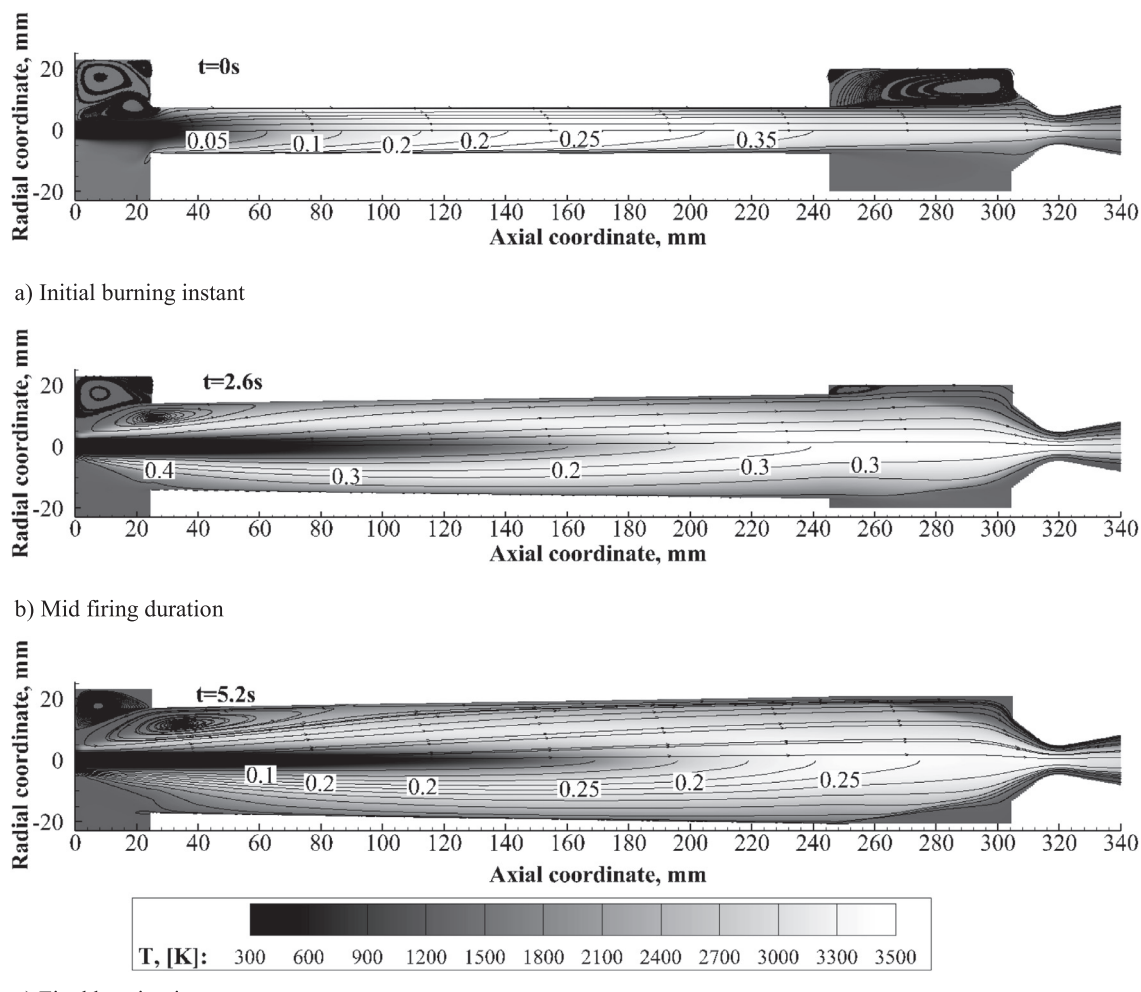


Fig. 17. Total temperature contours plot with overlapped streamlines (top half) and mixture-fraction isolines (bottom half) in the transient simulation of Test 4.

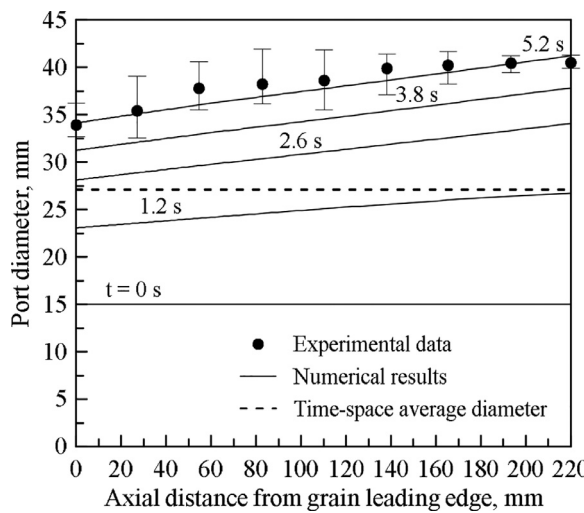


Fig. 18. Port-diameter evolution over time.

4. Conclusions

A substantial improvement of the liquefying-fuel surface boundary-condition statement employed in the numerical model previously developed by the authors to simulate the internal ballistics of hybrid rocket engines burning paraffin-based fuels was presented. The existing CFD model is based on the key assumption that liquid paraffin at the supercritical pressure regime in the rocket combustion chamber behaves similarly to a gas, whereby single-phase RANS equations, with two additional transport equations for the average mixture fraction and its variance combined to the PDF turbulent combustion model and thermochemical equilibrium, were solved. On this frame, a suitable sub-model for the interaction between the gaseous flow and the grain surface is integrated to predict the fuel regression rate. Local mass, energy and mixture fraction balances are formulated in combination with a liquid entrainment model and an in-depth fuel pyrolysis description. This latter block is the novelty addressed here, which allows for the determination of the surface temperature, and the corresponding liquid fuel viscosity considered in the entrainment regression rate formulation, as part of the flowfield resolution, in fact making the entire numerical apparatus dependent upon only one parameter (i.e. the constant entrainment factor appearing in the entrainment regression equation); the latter can be determined through matching the regression rate measured in a reference firing test. Once the entrainment constant was determined, a series of numerical simulations were carried out at the constant port diameter measured in the reference test by varying the oxygen mass flow rate, with the aim of exploring the effect of the oxygen mass flux on the fuel vaporization, fuel entrainment and the ensuing flowfield. This allowed deriving an approximate expression of the total regression rate, which highlighted that the main influential parameters are the oxygen mass flux itself, the average gas density in the port and, on a lesser degree, the liquid fuel viscosity. In all the analysed cases the vaporization fraction of the total regression rate resulted to be on the order of few percents.

A number of experimental test cases, consisting in the ground firing of gaseous oxygen with paraffin-based fuel grains in a laboratory-scale hybrid rocket, operating at chamber pressure larger than the liquid wax critical condition, were numerically reproduced in order to validate the computational model. A good match of the regression rates calculated at the time and space averaged port diameter with the measured data is achieved, with the largest deviation being less than 5%. The mismatch increases with

the port diameter, and the reason for that is supposed to be due to the effects of the flow recirculation established in the port inlet zone, which penetrates further downstream as the port diameter gets larger.

Calculations performed at the average diameter, however, were proved inadequate to reproduce the axial consumption profile, and a transient simulation, composed of a series of quasi-steady state numerical cases, was carried out over the firing duration of the reference test. The obtained results show much better agreement with the grain port shape measured after the firing, yielding a maximum deviation in the inlet region of the grain less than 8%.

In conclusion, the presented liquefying fuel surface temperature calculation model was demonstrated to be computationally affordable, and more accurate than that previously developed assuming constant temperature, in representing the fuel surface behavior; however, with the purpose of improving the overall CFD approach prediction capabilities, a liquid entrainment model able to reproduce the phenomenon even in more complex flows, such as the one dominated by the flow recirculation, is needed. The development of such a refined model is the target of the next research step.

Declaration of Competing Interest

The authors declare that they have no known competing financial interests or personal relationships that could have appeared to influence the work reported in this paper.

CRediT authorship contribution statement

Carmine Carmicino: Conceptualization, Methodology, Validation, Data curation, Writing - review & editing. **Giuseppe Gallo:** Software, Writing - original draft. **Raffaele Savino:** Project administration, Supervision.

Acknowledgements

The first author would like to thank Toru Shimada (ISAS-JAXA) as the main idea behind the model presented in this article was conceived over his period of visiting Associate Professorship in ISAS.

Appendix A. Governing equations

The density-weighted (Favre-averaged) equations of mass and momentum balance are expressed in Cartesian tensor form, with the understanding that repeated indices mean summation, respectively as [52]:

$$\frac{\partial \bar{\rho}}{\partial t} + \frac{\partial}{\partial x_j} (\bar{\rho} \tilde{u}_j) = S_m \quad (A1)$$

$$\frac{\partial}{\partial t} (\bar{\rho} \tilde{u}_i) + \frac{\partial}{\partial x_j} (\bar{\rho} \tilde{u}_i \tilde{u}_j) = - \frac{\partial \bar{p}}{\partial x_i} + \frac{\partial \bar{\tau}_{ij}}{\partial x_j} + \frac{\partial}{\partial x_j} \left(-\bar{\rho} \bar{u}'_i \bar{u}'_j \right) \quad (A2)$$

where S_m is the mass source term used to model the liquid fuel mass entrainment. Here the bar denotes conventional time averaging, while the tilde denotes density-weighted averaging; $\bar{\tau}_{ij}$ is the

Table A1
Values of SST model constants [52].

Constant	Value	Constant	Value
σ_{k_1}	0.850	σ_{k_2}	1.00
σ_{ω_1}	0.500	σ_{ω_2}	0.856
β_1	0.075	β_2	0.0828
γ_1	0.553	γ_2	0.440
β^*	0.090		

stress tensor that is defined as:

$$\tau_{ij} = \mu \left[\left(\frac{\partial u_i}{\partial x_j} + \frac{\partial u_j}{\partial x_i} \right) - \frac{2}{3} \delta_{ij} \frac{\partial u_k}{\partial x_k} \right] \quad (\text{A3})$$

where δ_{ij} is the Kronecker delta. Symbols with prime indicate the corresponding quantity fluctuation. The term $\mathcal{R}_{ij} = -\overline{\rho u'_i u'_j}$, originating from the averaging operation, is known as the Reynolds stress tensor, and it needs to be modelled.

The SST turbulence model has been selected for its improved capability of predicting flows with separated regions. With the latter, the transport equations of the turbulence kinetic energy, k , and the specific dissipation rate, ω , are formulated as follows:

$$\frac{\partial}{\partial t} (\bar{\rho} k) + \frac{\partial}{\partial x_i} (\bar{\rho} \tilde{u}_i k) = \frac{\partial}{\partial x_j} \left[(\mu + \mu_t \sigma_k) \frac{\partial k}{\partial x_j} \right] + \mathcal{R}_{ij} \frac{\partial \tilde{u}_i}{\partial x_j} - \beta^* \bar{\rho} \omega k \quad (\text{A4})$$

$$\begin{aligned} \frac{\partial}{\partial t} (\bar{\rho} \omega) + \frac{\partial}{\partial x_i} (\bar{\rho} \tilde{u}_i \omega) \\ = \frac{\partial}{\partial x_j} \left[(\mu + \mu_t \sigma_\omega) \frac{\partial \omega}{\partial x_j} \right] + \bar{\rho} \frac{\alpha}{\mu_t} \mathcal{R}_{ij} \frac{\partial \tilde{u}_i}{\partial x_j} - \beta \bar{\rho} \omega^2 \\ + 2(1 - F_1) \bar{\rho} \sigma_{\omega_2} \frac{1}{\omega} \frac{\partial k}{\partial x_i} \frac{\partial \omega}{\partial x_j} \end{aligned} \quad (\text{A5})$$

in which the Reynolds stress is modelled using the Boussinesq approximation:

$$\mathcal{R}_{ij} = \mu_t \left[\left(\frac{\partial \tilde{u}_i}{\partial x_j} + \frac{\partial \tilde{u}_j}{\partial x_i} \right) - \frac{2}{3} \delta_{ij} \frac{\partial \tilde{u}_l}{\partial x_l} \right] - \frac{2}{3} \bar{\rho} k \delta_{ij} \quad (\text{A6})$$

The turbulent viscosity, μ_t , is expressed as follows:

$$\mu_t = \frac{\bar{\rho} k}{\omega} \frac{1}{\max(1; \frac{\Omega F_2}{0.31\omega})} \quad (\text{A7})$$

where the function F_2 is defined, depending on the distance from the wall ξ , as

$$F_2 = \tanh(\Phi_2^2) \quad (\text{A8})$$

with

$$\Phi_2 = \max \left(\frac{2\sqrt{k}}{0.09\omega y}; \frac{500\mu}{\bar{\rho}\omega\xi^2} \right) \quad (\text{A9})$$

The coefficient α is given by

$$\alpha = \gamma \frac{1/9 + Re_t/2.95}{1 + Re_t/2.95} \quad (\text{A10})$$

where $Re_t = \bar{\rho}k/\mu\omega$ is the turbulent Reynolds number. The blending function F_1 takes the value of 1 on the wall and tends to zero at the boundary layer edge, being defined as

$$F_1 = \tanh(\Phi_1^4) \quad (\text{A11})$$

with

$$\Phi_1 = \min \left[\max \left(\frac{\sqrt{k}}{0.09\omega\xi}; \frac{500\mu}{\bar{\rho}\omega\xi^2} \right); \frac{4\bar{\rho}\sigma_{\omega_2}k}{CD_{k\omega}\xi^2} \right] \quad (\text{A12})$$

where $CD_{k\omega}$ is the positive part of the last term in Eq. (A5) (cross-diffusion term):

$$CD_{k\omega} = \max \left(2\bar{\rho}\sigma_{\omega_2} \frac{1}{\omega} \frac{\partial k}{\partial x_j} \frac{\partial \omega}{\partial x_j}; 10^{-20} \right) \quad (\text{A13})$$

The model coefficients σ_k , σ_ω , β , γ are defined by blending the corresponding coefficients of the original $k-\omega$ model, denoted with

the subscript 1, with those of the transformed $k-\varepsilon$ model that are denoted with the subscript 2:

$$\begin{bmatrix} \sigma_k \\ \sigma_\omega \\ \beta \\ \gamma \end{bmatrix} = F_1 \begin{bmatrix} \sigma_{k_1} \\ \sigma_{\omega_1} \\ \beta_1 \\ \gamma_1 \end{bmatrix} + (1 - F_1) \begin{bmatrix} \sigma_{k_2} \\ \sigma_{\omega_2} \\ \beta_2 \\ \gamma_2 \end{bmatrix} \quad (\text{A14})$$

All the constant values employed in the model are listed in Table A 1.

The density-averaged mixture fraction transport equation is:

$$\frac{\partial}{\partial t} (\bar{\rho} \tilde{f}) + \frac{\partial}{\partial x_j} (\bar{\rho} \tilde{u}_j \tilde{f}) = \frac{\partial}{\partial x_j} \left(\frac{\mu_t}{Sc_t} \frac{\partial \tilde{f}}{\partial x_j} \right) + S_m \quad (\text{A15})$$

For the closure of the turbulence-chemistry interaction model, the variance of the mean mixture fraction, \tilde{f}^2 , is introduced and an additional equation for this quantity is written as follows:

$$\begin{aligned} \frac{\partial}{\partial t} (\bar{\rho} \tilde{f}^2) + \frac{\partial}{\partial x_j} (\bar{\rho} \tilde{u}_j \tilde{f}^2) \\ = \frac{\partial}{\partial x_j} \left(\frac{\mu_t}{Pr_t} \frac{\partial \tilde{f}^2}{\partial x_j} \right) + 2 \frac{\mu_t}{Pr_t} \left(\frac{\partial \tilde{f}}{\partial x_j} \right)^2 - 2\beta^* \bar{\rho} \omega \tilde{f}^2 \end{aligned} \quad (\text{A16})$$

The assumed shape of the PDF is:

$$B(f) = \frac{f^{a_1-1} (1-f)^{a_2-1}}{\int_0^1 x^{a_1-1} (1-x)^{a_2-1} dx} \quad (\text{A17})$$

in which the two parameters a_1 and a_2 are functions of the mean mixture fraction and its variance:

$$a_1 = \tilde{f} \left[\frac{\tilde{f}(1-\tilde{f})}{\tilde{f}^2} - 1 \right] \quad (\text{A18})$$

$$a_2 = (1 - \tilde{f}) \left[\frac{\tilde{f}(1-\tilde{f})}{\tilde{f}^2} - 1 \right] \quad (\text{A19})$$

The enthalpy form of the energy equation is solved by neglecting the term of viscous dissipation (the Brinkman number, $Br = U^2 Pr_t / \Delta H_w$, which is defined as the ratio between heat produced by viscous dissipation and heat transported by turbulent conduction at the wall, is, indeed, on the order of $5 \cdot 10^{-3}$) as well as the variation of pressure (which is approximately constant all over the combustion chamber except through the discharge nozzle where, however, adiabatic walls are imposed), and combining the conduction and species diffusion terms, the latter can be written as:

$$\frac{\partial}{\partial t} (\bar{\rho} \tilde{H}) + \frac{\partial}{\partial x_j} (\bar{\rho} \tilde{u}_j \tilde{H}) = \frac{\partial}{\partial x_j} \left(\frac{\mu_t}{Pr_t} \frac{\partial \tilde{H}}{\partial x_j} \right) + S_h \quad (\text{A20})$$

where the source term S_h includes the volumetric heat of phase change. Here the enthalpy of the fluid mixture is defined as the sum of the heat of formation and the sensible enthalpy:

$$H = \sum_j Y_j \left[H_j^0 + \int_{T_{ref}}^T c_{p,j}(T) dT \right] \quad (\text{A21})$$

where Y_j is the mass fraction of the j th species and H_j^0 is its formation enthalpy at the reference temperature T_{ref} .

Density-weighted mean temperature and individual species mole fractions are then obtained as functions of \tilde{f} , \tilde{f}^2 and \tilde{H} as yielded by the following equation

$$\tilde{\varphi} = \int_0^1 \varphi(f, \tilde{H}) B(f) df \quad (\text{A22})$$

where $\varphi(f, \tilde{H})$ represents the generic functional dependency of one of the above-mentioned parameters on the mixture fraction and

enthalpy, whereas the mean density is calculated as:

$$\frac{1}{\bar{\rho}} = \int_0^1 \frac{B(f)}{\rho(f, \tilde{H})} df \quad (A23)$$

Note that the enthalpy turbulent fluctuations are assumed independent from the enthalpy level, so that the selected PDF in Eq. (A17) does not change.

Appendix B. Simplified solution of the liquid layer equations

A simplified solution to the liquid layer equations is addressed in this Appendix. In the limit of infinite activation energy, melting and liquid-phase reactions are confined in a thin layer beneath the regressing surface so that material is lost only from the surface region; this simplification leads to a so-called ablation model [41] for which the liquid mass fraction is constant throughout the liquid layer and it is discontinuous at the surface. Assuming that the fuel thermophysical properties both in the liquid and solid state are constant with temperature, the first of Eqs. (15) reduces to the following equation for temperature, whereas the second is trivial and states that the liquid mass fraction is identically equal to 1:

$$\frac{d^2T}{d\xi^2} + \frac{1}{\delta_l} \frac{dT}{d\xi} = 0 \quad (B1)$$

in which $\delta_l = \alpha_l \rho_l / \rho_s \dot{r}$ is the liquid-layer characteristic thermal thickness. The solution of this equation is:

$$T(\xi) = C_1 + C_2 e^{-\frac{\xi}{\delta_l}} = 0 \quad (B2)$$

The two constants of integration C_1 and C_2 can be determined through the following boundary conditions:

$$\xi = 0 \rightarrow \dot{q}_w = -\lambda_l \left(\frac{dT}{d\xi} \right)_w + \rho_s \dot{r}_v \Delta h_p \quad (B3)$$

$$T(h) = T_m \quad (A4)$$

The first boundary condition is set at the regressing surface, and imposes that the heat exchanged to the wall is equal to the heat lost by conduction into the fuel and the heat required for the liquid pyrolysis; in fact, with the assumption that the latter process is concentrated at the surface, the relevant energy term, removed from the inner of the liquid layer, has to be accounted for in the wall energy balance. Upon substitution, the two constants are eliminated, and Eq. (B2) reads

$$T(\xi) = T_m + \frac{\delta_l}{\lambda_l} (\dot{q}_w - \rho_s \dot{r}_v \Delta h_p) \left(e^{-\frac{\xi}{\delta_l}} - e^{-\frac{h}{\delta_l}} \right) \quad (B5)$$

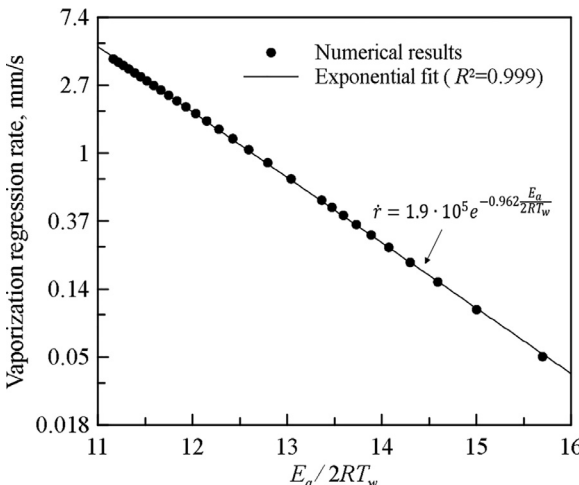


Fig. B1. Vaporization regression rate as a function of surface temperature.

in which the liquid layer thickness h is not known, and can be calculated through the energy balance at the solid/liquid interface:

$$-\lambda_l \left(\frac{\partial T}{\partial \xi} \right)_{\xi=h} = \frac{\lambda_s}{\delta_s} (T_m - T_a) + \rho_s L_m \dot{r} \quad (B6)$$

from which one obtains:

$$e^{-\frac{h}{\delta_l}} = \frac{\frac{\lambda_s}{\delta_s} (T_m - T_a) + \rho_s L_m \dot{r}}{\dot{q}_w - \rho_s \dot{r}_v \Delta h_p} \quad (B7)$$

By rearranging Eq. (B5) by means of Eq. (B7), the expression for the heat flux to the wall in Eq. (3) is eventually recovered; furthermore, using Eq. (3), it is immediate to show that the following relationship for the thickness of the liquid layer holds:

$$e^{-\frac{h}{\delta_l}} = \frac{c_s (T_m - T_a) + L_m}{c_l (T_w - T_m) + c_s (T_m - T_a) + L_m} \quad (B8)$$

Note that, as discussed in the text, this equation predicts that, as $\dot{r} \rightarrow 0$ (i.e. $\delta_l \rightarrow \infty$), the term on the right-hand side being a finite quantity, h tends to infinity. Moreover, in case $h = 0$, there is no vaporization, and Eq. (B8) accordingly implies that the surface temperature is equal to the melting temperature.

With the substitution of Eq. (B7) into Eq. (B5), and resorting, for the sake of brevity, to the positions: $\varphi = e^{-\frac{h}{\delta_l}}$, $\Delta T = T_w - T_m$, $\varepsilon = \xi/\delta_l$, the temperature profile assumes the linear form:

$$T(\epsilon) = T_w \left(1 - \frac{\Delta T}{T_w} \frac{1 - e^{-\epsilon}}{1 - \varphi} \right) \cong T_w \left(1 - \frac{\Delta T}{T_w} \frac{\epsilon}{1 - \varphi} \right) \quad (B9)$$

in which the exponential expansion up to the first-order term around $\epsilon \ll 1$ has been used. Hence, the activation energy factor E_a/RT can be approximated as follows:

$$\frac{E_a}{RT} = \frac{E_a}{RT_w} \frac{1}{1 - \frac{\Delta T}{T_w} \frac{\epsilon}{1 - \varphi}} \cong \frac{E_a}{RT_w} \left(1 + \frac{\Delta T}{T_w} \frac{\epsilon}{1 - \varphi} \right) \quad (B10)$$

and the integral in Eq. (9) can be analytically calculated considering that $Y = 1$:

$$\rho_s \dot{r}_v = \int_0^h \rho_l B_p e^{-E_a/RT} Y d\xi = \rho_l B_p e^{-\frac{E_a}{RT_w} \delta_l} \int_0^h e^{-\frac{E_a}{RT_w} \frac{\Delta T}{T_w} \frac{\epsilon}{1 - \varphi}} d\epsilon \quad (B11)$$

whereby, as $e^{-\frac{E_a}{RT_w} \frac{\Delta T}{T_w} \frac{h/\delta_l}{1 - \varphi}} \cong e^{-\frac{E_a}{RT_w} \frac{\Delta T}{T_w}} \ll 1$, by means of Eq. (B8), one finally obtains the following approximate expression for the vaporization component of regression rate:

$$\dot{r}_v = \delta_l B_p \frac{e^{-\frac{E_a}{RT_w}} \cdot c_l T_w}{\frac{E_a}{RT_w} [c_l (T_w - T_m) + c_s (T_m - T_a) + L_m]} \quad (B12)$$

If $h = h_{max}$, regression rate is entirely due to vaporization, and Eq. (B12) becomes:

$$\dot{r}_v = \sqrt{\alpha_l \frac{\rho_l}{\rho_s} B_p \frac{c_l T_w}{\frac{E_a}{RT_w} [c_l (T_w - T_m) + c_s (T_m - T_a) + L_m]}} e^{-\frac{E_a}{2RT_w}} \quad (B13)$$

Note that, in case of a classical polymer, which does not melt on the surface while undergoes pyrolysis, this equation reduces to:

$$\dot{r} = \sqrt{\frac{\alpha_s B_p}{\frac{E_a}{RT_w} \left[1 - \frac{T_a}{T_w} + \frac{\Delta h_p}{c_s T_w} \right]}} e^{-\frac{E_a}{2RT_w}} \quad (B14)$$

which is practically coincident with the result of the complete calculations given by Lengelle [53].

Eq. (B13) predicts that the vaporization regression rate obtained at the maximum liquid layer thickness varies with temperature essentially following a negative exponential: $\dot{r}_v \propto e^{-\frac{E_a}{2RT_w}}$; in fact,

the data in Fig. 3a have been redrawn in Fig. B1 as a function of the parameter $E_a/2RT_w$ in logarithmic scale. The numerical data points are best fit with an exponential coefficient of -0.962 and a constant pre-exponential factor yielding a squared correlation index of 0.999 , thus demonstrating the validity of Eq. (B13) in which the temperature dependence of the pre-exponential factor is dropped.

References

- [1] D. Altman, R. Humble, Hybrid Rocket Propulsion Systems, in: R.W. Humble, G.N. Henry, W.J. Larson (Eds.), *Space Propulsion Analysis and Design*, 1st Ed., McGraw-Hill, New York, 1995, pp. 365–370.
- [2] Leccese, C., Cavallini, E., Pizzarelli, M. State of Art and Current Challenges of the Paraffin-Based Hybrid Rocket Technology, AIAA Paper 2019-4010, 2019. doi:<https://doi.org/10.2514/6.2019-4010>.
- [3] A. Karabeyoglu, G. Zilliac, B.J. Cantwell, S. De Zilwa, P. Castellucci, Scale-Up Tests of High Regression Rate Paraffin-Based Hybrid Rocket Fuels, *J. Propuls. Power* 20 (6) (2004) 1037–1045, doi:[10.2514/1.3340](https://doi.org/10.2514/1.3340).
- [4] A. Mazzetti, L. Merotto, G. Pinarello, Paraffin-Based Hybrid Rocket Engines Applications: A Review and a Market Perspective, *Acta Astronaut.* 126 (2016) 286–297, doi:[10.1016/j.actaastro.2016.04.036](https://doi.org/10.1016/j.actaastro.2016.04.036).
- [5] D. Altman, A. Holzman, Overview and History of Hybrid Rocket Propulsion, in: K. Kuo, M. Chiaverini (Eds.), *Fundamentals of Hybrid Rocket Combustion and Propulsion*, *Prog. Astronaut. Aeronaut.*, Vol. 218, AIAA, Reston, VA, 2007, pp. 1–36.
- [6] C. Carmicino, Special Issue: Advances in Hybrid Rocket Technology and Related Analysis Methodologies, *Aerospace* 6 (12) (2019) 128, doi:[10.3390/aerospace6120128](https://doi.org/10.3390/aerospace6120128).
- [7] M.A. Karabeyoglu, D. Altman, B.J. Cantwell, Combustion of liquefying hybrid propellants: Part 1 General Theory, *J. Propuls. Power* 18 (3) (2002) 610–620, doi:[10.2514/2.5975](https://doi.org/10.2514/2.5975).
- [8] M.A. Karabeyoglu, B.J. Cantwell, Combustion of liquefying hybrid propellants: part 2, stability of liquid films, *J. Propuls. Power* 18 (3) (2002) 621–630, doi:[10.2514/2.5976](https://doi.org/10.2514/2.5976).
- [9] Chandler, A., Jens, E., Cantwell, B. J., and Hubbard, G. S., “Visualization of the Liquid Layer Combustion of Paraffin Fuel for Hybrid Rocket Applications,” AIAA paper 2012-3961, July 2012. doi:<https://doi.org/10.2514/6.2012-3961>.
- [10] E.T. Jens, A.C. Karp, V.A. Miller, G.S. Hubbard, B.J. Cantwell, Experimental Visualization of Hybrid Combustion: Results at Elevated Pressures, *J. Propuls. Power* 36 (1) (2020) 1–14, doi:[10.2514/1.B37416](https://doi.org/10.2514/1.B37416).
- [11] A. Petrarolo, M. Kobald, Evaluation Techniques for Optical Analysis of Hybrid Rocket Propulsion, *J. Fluid Sci. Technol.* 11 (4) (2016) 1–20, doi:[10.1299/jfst.2016jfst0028](https://doi.org/10.1299/jfst.2016jfst0028).
- [12] A. Petrarolo, M. Kobald, S. Schlechtriem, Understanding Kelvin-Helmholtz instability in paraffin-based hybrid rocket fuels, *Exp. Fluids* 59 (62) (2018) 1–16, doi:[10.1007/s00348-018-2516-1](https://doi.org/10.1007/s00348-018-2516-1).
- [13] G.A. Marxman, M. Gilbert, Turbulent boundary layer combustion in the hybrid rocket, Ninth International Symposium on Combustion, Academic Press, 1963, pp. 371–383, doi:[10.1016/S0082-0784\(63\)80046-6](https://doi.org/10.1016/S0082-0784(63)80046-6).
- [14] C. Carmicino, F. Scaramuzzino, A. Russo Sorge, Trade-off Between Paraffin-Based and Aluminum-Loaded HTPB Fuels to Improve Performance of Hybrid Rocket Fed with N2O, *Aerospace Sci. Technol.* 37 (2014) 81–92, doi:[10.1016/j.ast.2014.05.010](https://doi.org/10.1016/j.ast.2014.05.010).
- [15] M. Kobald, C. Schmierer, H.K. Ciezki, S. Schlechtriem, E. Toson, L.T. De Luca, Viscosity and Regression Rate of Liquefying Hybrid Rocket Fuels, *J. Propuls. Power* 33 (5) (2017) 1245–1251, doi:[10.2514/1.B36207](https://doi.org/10.2514/1.B36207).
- [16] G.D. Di Martino, S. Munguerra, C. Carmicino, R. Savino, D. Cardillo, F. Battista, M. Invigorito, G. Elia, Two-Hundred-Newton Laboratory-Scale Hybrid Rocket Testing for Paraffin Fuel-Performance Characterization, *J. Propuls. Power* 35 (1) (2019) 224–235, doi:[10.2514/1.B37017](https://doi.org/10.2514/1.B37017).
- [17] K. Veale, S. Adali, J. Pitot, M. Brooks, A Review of the Performance and Structural Considerations of Paraffin Wax Hybrid Rocket Fuels With Additives, *Acta Astronaut.* 141 (2017) 196–208 December, doi:[10.1016/j.actaastro.2017.10.012](https://doi.org/10.1016/j.actaastro.2017.10.012).
- [18] G.D. Di Martino, C. Carmicino, S. Munguerra, R. Savino, The Application of Computational Thermo-Fluid-Dynamics to the Simulation of Hybrid Rocket Internal Ballistics with Classical or Liquefying Fuels: A Review, *Aerospace* 6 (5) (2019) 56, doi:[10.3390/aerospace6050056](https://doi.org/10.3390/aerospace6050056).
- [19] V. Sankaran, Computational Fluid Dynamics Modeling of Hybrid Rocket Flow-fields, in: K. Kuo, M. Chiaverini (Eds.), *Fundamentals of Hybrid Rocket Combustion and Propulsion*, *Prog. Astronaut. Aeronaut.*, Vol. 218, AIAA, Reston, VA, 2007, pp. 323–349.
- [20] M. Lazzarin, M. Faenza, F. Barato, N. Bellomo, A. Bettella, D. Pavarin, Computational Fluid Dynamics Simulation of Hybrid Rockets of Different Scales, *J. Propuls. Power* 31 (5) (2015) 1458–1469, doi:[10.2514/1.B35528](https://doi.org/10.2514/1.B35528).
- [21] G. Ranuzzi, D. Cardillo, M. Invigorito, Numerical Investigation of a N2O-Paraffin Hybrid Rocket Engine Combusting Flowfield, in: Proceedings of 6th European Conference for Aeronautics and Space Sciences (EUCASS), Krakow, Poland, 2015 29 Jun. – 3 Jul.
- [22] D. Cardillo, F. Battista, G. Elia, G.D. Di Martino, S. Munguerra, R. Savino, Design and Testing of a Paraffin-based Hybrid Rocket Demonstrator, in: Proceedings of Space Propulsion Conference 2018, Seville, Spain, 2018, pp. SP2018-S00508. 14–18 May.
- [23] D. Bianchi, B. Betti, F. Nasuti, C. Carmicino, Simulation of Gaseous Oxygen/Hydroxyl-Terminated Polybutadiene Hybrid Rocket Flowfields and Comparison with Experiments, *J. Propuls. Power* 31 (3) (2015) 919–929, doi:[10.2514/1.B35587](https://doi.org/10.2514/1.B35587).
- [24] G.D. Di Martino, C. Carmicino, R. Savino, Transient Computational Thermo-fluid-Dynamical Simulation of Hybrid Rocket Internal Ballistics, *J. Propuls. Power* 33 (6) (2017) 1395–1409, doi:[10.2514/1.B36425](https://doi.org/10.2514/1.B36425).
- [25] I. Mantilla, L. Gomez, R. Mohan, O. Shoham, G. Kouba, R. Roberts, Experimental Investigation of Liquid Entrainment in Gas in Horizontal Pipes, in: Proceedings of the ASME 2009 Fluids Engineering Division Summer Meeting, Volume 1: Symposia, Parts A, B and C, Vail, Colorado, USA, ASME, 2009, pp. 943–969. August 2–6, doi:[10.1115/FEDSM2009-78420](https://doi.org/10.1115/FEDSM2009-78420).
- [26] M. Adachi, T. Shimada, Liquid Films Instability Analysis of Liquefying Hybrid Rocket Fuels Under Supercritical Conditions, *AIAA Journal* 53 (6) (2015) 1578–1589, doi:[10.2514/1.J053459](https://doi.org/10.2514/1.J053459).
- [27] Knol, I. M., Maicke, B. A., “Simulation of Surface Instabilities in Liquefying Hybrid Rocket Fuels”, AIAA paper 2019-3919. Aug. 2019. doi:<https://doi.org/10.2514/6.2019-3919>.
- [28] Leccese, G., Bianchi, D., Nasuti, F., “Modeling and Simulation of Paraffin-Based Hybrid Rocket Internal Ballistics,” AIAA paper 2018-4533. Jul. 2018. doi:<https://doi.org/10.2514/6.2018-4533>.
- [29] Tindaro Migliorino, M., Bianchi, D., Nasuti, F., “Predictive CFD Model for Internal Ballistics of Hybrid Rocket Engines using Supercritical Paraffin-wax and Oxygen,” AIAA paper 2019-4261, Aug. 2019. doi:<https://doi.org/10.2514/6.2019-4261>.
- [30] D. Bianchi, F. Nasuti, D. Delfini, Modeling of Gas-Surface Interface for Paraffin-Based Hybrid Rocket Fuels in Computational Fluid Dynamics Simulations, *Progress in Propulsion Physics* 11 (2019) 3–24, doi:[10.1051/eucass/201911003](https://doi.org/10.1051/eucass/201911003).
- [31] G. Leccese, D. Bianchi, F. Nasuti, K.J. Stober, N. Pavan, B. Cantwell, Simulations of Paraffin-Based Hybrid Rocket Engines and Comparison with Experiments, *AIAA paper* (2017) 2017–4737 Jul, doi:[10.2514/6.2017-4737](https://doi.org/10.2514/6.2017-4737).
- [32] G.D. Di Martino, S. Munguerra, C. Carmicino, R. Savino, Computational fluid-dynamical modeling of the internal ballistics of paraffin-fueled hybrid rocket, *Aerospace Sci. Technol.* 89 (2019) 431–444, doi:[10.1016/j.ast.2019.04.019](https://doi.org/10.1016/j.ast.2019.04.019).
- [33] J.J. Marano, G.D. Holder, General Equation for Correlating the Thermophysical Properties of n-Paraffins, n-Olefins, and Other Homologous Series. 2. Asymptotic Behavior Correlations for PVT Properties, *Ind. Eng. Chem. Res.* 36 (5) (1997) 1895–1907, doi:[10.1021/ie960512f](https://doi.org/10.1021/ie960512f).
- [34] A.J. Chorin, Numerical Solution of Navier-Stokes Equations, *Math. Comput.* 22 (104) (1968) 745–745, doi:[10.1090/S0025-5718-1968-0242392-2](https://doi.org/10.1090/S0025-5718-1968-0242392-2).
- [35] F.R. Menter, Two-Equation Eddy-Viscosity Turbulence Models for Engineering Applications, *AIAA Journal* 32 (8) (1994) 1598–1605, doi:[10.2514/3.12149](https://doi.org/10.2514/3.12149).
- [36] C.E. Wooldridge, G.A. Marxman, R.J. Kier, Investigation of Combustion Instability in Hybrid Rockets, *NASACR NAS 1-7310* (1969).
- [37] Y.R. Sivathanu, G.M. Faeth, Generalized State Relationships for Scalar Properties in Non-Premixed Hydrocarbon/Air Flames, *Combust. Flame* 82 (2) (1990) 211–230, doi:[10.1016/0010-2180\(90\)90099-D](https://doi.org/10.1016/0010-2180(90)90099-D).
- [39] M. Hazewinkel, Beta-distribution, in: M. Hazewinkel (Ed.), *Encyclopedia of Mathematics*, Springer, Netherlands, 2001.
- [39] W.P. Jones, J.H. Whitelaw, Calculation Methods for Reacting Turbulent Flows: A Review, *Combust. Flame* 48 (Dec. 1982) 1–26, doi:[10.1016/0010-2180\(82\)90112-2](https://doi.org/10.1016/0010-2180(82)90112-2).
- [40] S. Gordon, B.J. McBride, Computer program of complex chemical equilibrium compositions and applications, *NASA Reference Publication* 1311 (1994).
- [41] J.E.J. Staggs, A Theoretical Investigation into Modelling Thermal Degradation of Solids Incorporating Finite-Rate Kinetics, *Combust. Sci. Technol.* 123 (1997) 261–285, doi:[10.1080/00102290708935631](https://doi.org/10.1080/00102290708935631).
- [42] J.J. Marano, G.D. Holder, A General Equation for Correlating the Thermophysical Properties of n-Paraffins, n-Olefins, and Other Homologous Series. 3. Asymptotic Behavior Correlations for Thermal and Transport Properties, *Ind. Eng. Chem. Res.* 36 (6) (1997) 2399–2408, doi:[10.1021/ie9605138](https://doi.org/10.1021/ie9605138).
- [43] A. Karabeyoglu, B.J. Cantwell, J. Stevens, Evaluation of Homologous Series of Normal-Alkanes as Hybrid Rocket Fuels, *AIAA paper* (2005) 2005-3908, doi:[10.2514/6.2005-3908](https://doi.org/10.2514/6.2005-3908).
- [44] C. Berna, A. Escrivá, J.L. Muñoz-Cobo, L.E. Herranz, Review of droplet entrainment in annular flow: Interfacial waves and onset of entrainment, *Prog. Nucl. Energy* 74 (2014) 14–43, doi:[10.1016/j.pnucene.2014.01.018](https://doi.org/10.1016/j.pnucene.2014.01.018).
- [45] C. Carmicino, A. Russo Sorge, Influence of a Conical Axial Injector on Hybrid Rocket Performance, *J. Propuls. Power* 22 (5) (2006) 984–995, doi:[10.2514/1.19528](https://doi.org/10.2514/1.19528).
- [46] C. Carmicino, Acoustics, Vortex Sheding, and Low-Frequency Dynamics Interaction in an Unstable Hybrid Rocket, *J. Propuls. Power* 25 (6) (2009) 1322–1335, doi:[10.2514/1.42869](https://doi.org/10.2514/1.42869).
- [47] C. Carmicino, A. Russo Sorge, Experimental Investigation into the Effect of Solid-Fuel Additives on Hybrid Rocket Performance, *J. Propuls. Power* 31 (2) (2015) 699–713, doi:[10.2514/1.B35383](https://doi.org/10.2514/1.B35383).
- [48] G.N. Abramovich, *General Properties of Turbulent Jets*, MIT Press, Cambridge, MA, 1963, pp. 3–46.
- [49] D. Bianchi, F. Nasuti, C. Carmicino, Hybrid Rockets with Axial Injector: Port Diameter Effect on Fuel Regression Rate, *J. Propuls. Power* 32 (4) (2016) 984–996, doi:[10.2514/1.B36000](https://doi.org/10.2514/1.B36000).
- [50] M.A. Karabeyoglu, B.J. Cantwell, G. Zilliac, Development of Scalable Space-Time Averaged Regression Rate Expressions for Hybrid Rockets, *J. Propuls. Power* 33 (4) (2007) 737–747, doi:[10.2514/1.19226](https://doi.org/10.2514/1.19226).

- [51] J. Messineo, K. Kitagawa, C. Carmicino, T. Shimada, C. Paravan, Reconstructed Ballistic Data Versus Wax Regression-Rate Intrusive Measurement in a Hybrid Rocket, *J. Spacecr. Rockets* 57 (6) (2020) 1295–1308, doi:[10.2514/1.A34695](https://doi.org/10.2514/1.A34695).
- [52] T. Cebeci, *Analysis of Turbulent Flows*, 2nd Revised and Expanded ed., Elsevier, Oxford, England, U.K., 2004, pp. 32–38.
- [53] G. Lengellé, *Solid-Fuel Pyrolysis Phenomena and Regression Rate, Part 1: Mechanisms*, in: K. Kuo, M. Chiaverini (Eds.), *Fundamentals of Hybrid Rocket Combustion and Propulsion*, Prog. Astronaut. Aeronaut., Vol. 218, AIAA, Reston, VA, 2007, pp. 127–163.